

Time Evolution within a Comoving Window: Scaling of signal fronts and magnetization plateaus after a local quench in quantum spin chains

V Zauner^{1,2,3}, M Ganahl^{1,4}, H G Evertz¹, T Nishino³

¹Institute of Theoretical and Computational Physics, Graz University of Technology, 8010 Graz, Austria

²Vienna Center for Quantum Technology, University of Vienna, 1090 Vienna, Austria

³Department of Physics, Graduate School of Science, Kobe University, Kobe 657-8501, Japan

⁴Perimeter Institute for Theoretical Physics, Waterloo, ON N2L 2Y5, Canada

E-mail: valentin.zauner@univie.ac.at

Abstract. We present a modification of Matrix Product State time evolution to simulate the propagation of signal fronts on infinite one-dimensional systems. We restrict the calculation to a window moving along with a signal, which by the Lieb-Robinson bound is contained within a light cone. Signal fronts can be studied unperturbed and with high precision for much longer times than on finite systems. Entanglement inside the window is naturally small, greatly lowering computational effort. We investigate the time evolution of the transverse field Ising (TFI) model and of the $S = 1/2$ XXZ antiferromagnet in their symmetry broken phases after several different local quantum quenches.

In both models, we observe distinct magnetization plateaus at the signal front for very large times, resembling those previously observed for the particle density of tight binding (TB) fermions. We show that the normalized difference to the magnetization of the ground state exhibits similar scaling behaviour as the density of TB fermions. In the XXZ model there is an additional internal structure of the signal front due to pairing, and wider plateaus with tight binding scaling exponents for the normalized excess magnetization. We also observe parameter dependent interaction effects between individual plateaus, resulting in a slight spatial compression of the plateau widths.

In the TFI model, we additionally find that for an initial Jordan-Wigner domain wall state, the complete time evolution of the normalized excess longitudinal magnetization agrees exactly with the particle density of TB fermions.

Keywords: Strongly Correlated Systems, Tensor Network States, Quantum Quenches, Unitary Time Evolution, Particle Propagation, Integrable Systems

PACS numbers: 75.10.Pq, 02.30.Ik, 05.60.Gg 75.40.Mg,

Submitted to: *New J. Phys.*

1. Introduction

Signal propagation in one-dimensional (1D) strongly interacting quantum lattice systems has been of longstanding general interest in both condensed matter and quantum-computational physics, where it provides a basis for coherent information transfer via quantum wires. A signal can be created, e.g., as a local excitation from a stationary state, or as a domain wall or a topological excitation [1, 2]. Often hard to pursue by analytical methods, many studies have become feasible in 1D due to Matrix Product State (MPS) [3, 4, 5] based numerical methods [6, 7, 8]. Thus the non-equilibrium time evolution of such signals after global [9, 10, 11, 12, 13, 14, 15, 16, 17, 18, 19, 20, 21, 22, 23] and local [24, 25, 26, 27, 28, 29, 30, 31, 32, 33, 34, 35, 36, 37, 38, 39, 40, 41, 42, 43] quantum quenches has been the subject of intense theoretical interest in recent years. In particular for tight binding (TB) fermions initially in a domain wall (DW) state, intriguing plateaus in the fermion density have been found to develop at large times with well defined scaling behaviour [41, 42, 43] and have only been fully understood recently [44].

If an initial state for such a study is prepared within a *finite* system, boundary effects such as Friedel oscillations interfere with a passing signal. System boundaries also limit the time span for signal tracing before non-trivial reflections occur at the boundaries. The maximum time is even more severely restricted by entanglement which develops across the system and which requires a computational effort that can drastically increase with time [45, 46]. This has greatly hampered the analysis of large time asymptotic behaviour [19, 28, 34]. Boundary effects do not appear in *infinite* systems, for which the ground state and its time evolution can be efficiently calculated with MPS methods [6, 47, 48, 49]. However, these methods require complete translation invariance and can therefore not be applied to study signal propagation.

In this paper we present a simple method to simulate the propagation of local signals on an infinite chain using MPS time evolution, without any finite size effects distorting the signal front. For related approaches to boundary effects, see [50, 51, 52, 53]. We study the time evolution of the Transverse Field Ising (TFI) model and of the spin-1/2 XXZ chain after *local* quantum quenches up to large times, which were not accessible before using conventional MPS techniques. In both models we observe distinct magnetization plateaus developing over time close to the signal front similar to the case of TB fermions [41, 42, 44], and which also exhibit similar asymptotic scaling. Surprisingly we find an exact agreement at all times and positions between the magnetization in the TFI model and the density of TB fermions for a particular type of signal. For the XXZ chain we observe interaction effects between individual plateaus, which can be tuned via the model parameters.

For our method we consider a spin chain of infinite size with nearest neighbour interactions, initially prepared in a state – such as the ground state – which is translation invariant for sites $n > n_0$ to the right of some site n_0 . At time zero, the system is excited by a quantum quench like one or more spin flips at sites $n \leq n_0$ or a modification of

the Hamiltonian at $n \leq n_0$. For local interactions it is known from the Lieb-Robinson bound [54, 55] that wave fronts generated by such quenches can at most propagate with a characteristic maximum velocity v_{\max} , i.e. within a "light cone" even in a non-relativistic system as recently also seen experimentally [1]. Any correlations beyond the light cone are exponentially suppressed. In the following we will consider right moving signals for the sake of concreteness.

2. Method

Our approach is to introduce a division of the system into three parts, namely a *comoving window* (CMW) – which moves towards the right with the wave front – and two half-infinite parts, a uniform one in front (i.e. to the right) of the window, and an arbitrary one to the rear. The window is chosen wide enough to contain the complete signal front, including the exponentially damped part to the right of the main front, to high precision. The signal therefore does not affect the uniform system to the right of the window. Likewise, when the window moves with v_{\max} , modifications in the rear part do not affect the CMW and need not be calculated. The method is therefore fit for studying fronts of propagating signals, in particular those generated by local quenches. Since bipartite entanglement [14, 26, 56, 57] spreads at most with v_{\max} , the bipartite entanglement entropy is significantly lower around the wave front than in the bulk, allowing for reduced computational effort when using the CMW.

We mark the left and right boundary of the CMW with indices ℓ and r respectively and divide the system into left part $j \leq \ell$, CMW $\ell + 1 \leq j \leq r$, and right part $j \geq r + 1$. The Hamiltonian $\hat{H} = \sum_j \hat{h}_{j,j+1}$ subdivides correspondingly into

$$\hat{H} = \hat{H}_L + \hat{h}_{\ell,\ell+1} + \hat{H}_M + \hat{h}_{r,r+1} + \hat{H}_R. \quad (1)$$

Low energy states of the overall system are well approximated by Matrix Product States (MPS) [4, 5] and we write the wave function as an MPS in the so-called mixed canonical form as

$$\psi(\{s_j\}) = \dots L^{s_{\ell-1}} L^{s_{\ell}} A^{s_{\ell+1}} \dots A^{s_k} \lambda^k B^{s_{k+1}} \dots B^{s_r} R^{s_{r+1}} R^{s_{r+2}} \dots, \quad (2)$$

where s_j labels the spins, $L^{s_j \leq \ell}$ are left-orthogonal matrices ($\sum_{s_{\ell}} L^{s_j \dagger} L^{s_j} = \mathbb{1}$) defined on the left part, $R^{s_{r+1} \leq j}$ are right-orthogonal matrices ($\sum_{s_j} R^{s_j} R^{s_j \dagger} = \mathbb{1}$) defined on the right part, $A^{s_{\ell+1} \leq j \leq r}$ and $B^{s_{\ell+1} \leq j \leq r}$ are left- and right-orthogonal matrices respectively defined inside the CMW, and $\lambda^{\ell \leq k \leq r}$ are diagonal matrices containing the Schmidt values of a bipartition at bond $(k, k + 1)$. For a finite system, the left and right ends of (2) are terminated by contractions with boundary vectors; we however consider the infinite size limit.

The matrices R^{s_j} describe the uniform half-infinite system in the front and are therefore constrained to be translation invariant. We use a 2-site unit cell, i.e. $R^{s_{j+2}} = R^{s_j}$. The matrices A^{s_j} and B^{s_j} describe the CMW and are site dependent. For the matrices L^{s_j} , which describe the left part, we impose no uniformity restrictions. They represent initial conditions for the left boundary of the CMW and remain unchanged

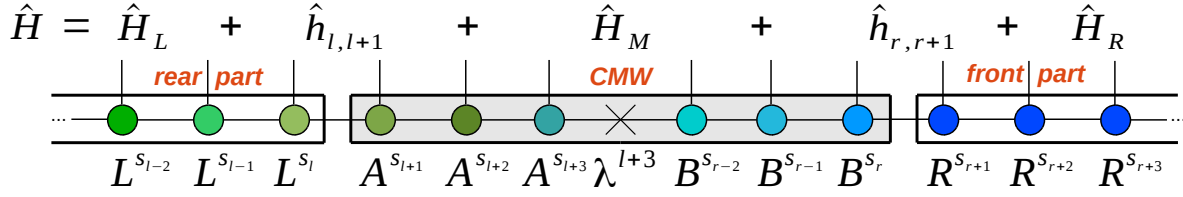


Figure 1. Graphical representation of the MPS describing the overall system state, which is divided into comoving window (CMW), left and right part.

throughout the simulation. Additional matrices are added to this collection of L^{s_j} whenever the CMW is moved.

Let us consider one step of unitary time evolution for the entire system. Inside the CMW, between sites $\ell + 1$ and r , we employ time dependent Density Matrix Renormalization Group (tDMRG [8]), using a second order even-odd Suzuki-Trotter decomposition [58] with local operators $\hat{u}_{j,j+1}(\tau) = e^{-i\tau\hat{h}_{j,j+1}}$ and small time steps τ .

In order to connect time evolution inside and outside the CMW we introduce two different approaches, which we now sketch for the case of the right (front) and the left (rear) boundary respectively. Details can be found in Appendix A.

In *Method I (Uniform Update)*, applied to the right boundary, the matrices R^{s_j} of the right part are first updated by infinite system Time Evolving Block Decimation (iTEBD [47]). We then evolve the junction bond $(r, r + 1)$ by applying $\hat{u}_{r,r+1}$ and we exploit right-orthogonality of $R^{s_{r+1}}$ to update B^{s_r} and to ensure gauge consistency of MPS matrices around the junction bond.

For *Method II (Renormalized Update)*, applied to the left boundary, we adapt the algorithm of Cazalilla and Marston [59] (Method II is similar to the algorithm introduced in [50, 51], see [53]) and construct a renormalized representation for $H_L + h_{\ell, \ell+1}$ to approximate the evolution of the left part and the left junction bond $(\ell, \ell + 1)$, such that all changes in the left part are compressed into the boundary matrix $A^{s_{\ell+1}}$, and the matrices $L^{s_j \leq \ell}$ remain unchanged.

The Uniform Update has some immediate advantages. It is easier to implement and it is also applicable in case of a time dependent H_R . It does however require translation invariance of the right part. The Renormalized Update does not preserve the structure of the Suzuki-Trotter decomposition at the boundary and therefore continually introduces small perturbations there. In Appendix D we compare both methods to analytical results and to a reference simulation on a very large stationary lattice and show that both methods work well. As errors in our new Uniform Update, when applied to the right boundary, are only of order $O(10^{-8})$ and thus smaller by several orders of magnitude than for the Renormalized Update, we use the Uniform Update for the right boundary.

For the left boundary, the simplest approach is to disconnect the left part by setting $\hat{h}_{\ell, \ell+1} = 0$, which already works quite well (see Appendix D) when the window moves with v_{\max} , as then any perturbations are confined to the neighbourhood of the rear boundary. Since perturbations there are however smallest with the Renormalized

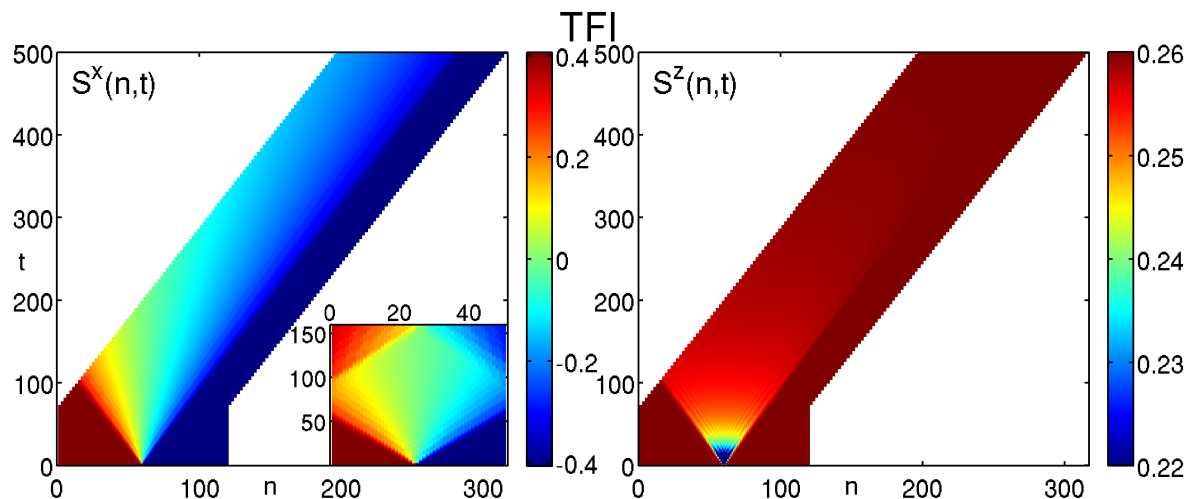


Figure 2. Time evolution of magnetizations $S^x(n,t)$ and $S^z(n,t)$ in the TFI model at $h = 0.45$ after a JW excitation. We show times only up to $t = 500$ in order to keep structures resolvable to the eye, while simulations were performed up to $t = 1000$. *Inset:* Time evolution of $S^x(n,t)$ without window movement, showing eventual reflections.

Update, we use this method for the left boundary in the present paper, For further details on the boundary updates and how to move the CMW along with a propagating signal see Appendix A.

3. Results

3.1. Transverse Field Ising (TFI) model

The spin-1/2 TFI model [9, 10, 11, 12, 13, 14, 15, 16, 17, 18, 24, 25, 26, 27] on an infinite chain defined by

$$\hat{H} = - \sum_n \hat{S}_n^x \hat{S}_{n+1}^x - h \sum_n \hat{S}_n^z \quad (3)$$

can be solved exactly [60, 61] (see also Appendix B), and the time evolution of local observables can in principle be calculated [11, 10]. For the *longitudinal* magnetization $S^x(n,t)$ (order parameter), analytical calculations are however difficult and some results have become available in the literature only recently [10, 12], but to our knowledge not for local quenches on infinite systems. In the ferromagnetic phase $h < h_c = 0.5$ the ground state is twofold degenerate and there is long range order in S^x .

We prepare the system in the maximally symmetry broken ground state $|\Downarrow\rangle$ (Appendix A.1) with $S_{\text{GS}}^x := \langle \hat{S}_n^x \rangle < 0$ using iDMRG [6, 48] and study the time evolution of several initial states excited from $|\Downarrow\rangle$. In figure 2 we show results for a Jordan-Wigner (JW) excitation

$$(c_{n_0}^\dagger + c_{n_0}) |\Downarrow\rangle = \prod_{n < n_0} (-2\hat{S}_n^z)(2\hat{S}_{n_0}^x) |\Downarrow\rangle \quad (4)$$

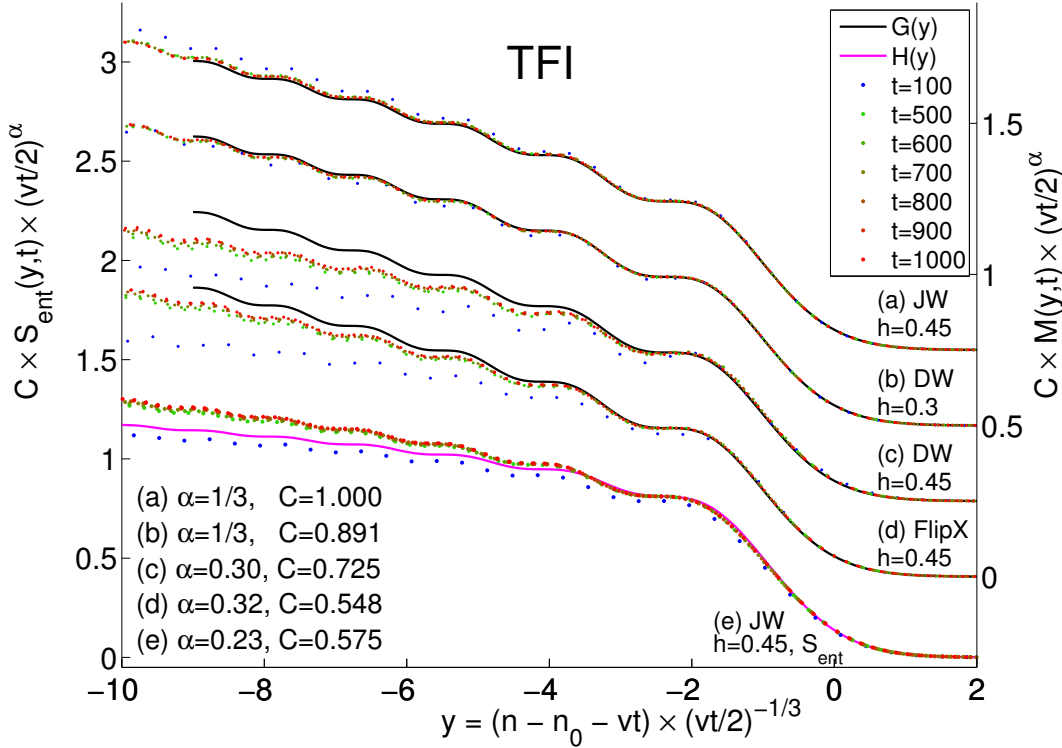


Figure 3. Scaled normalized excess magnetization $M(y,t)$ (right axis) and bipartite entanglement entropy $S_{\text{ent}}(y,t)$ (bottom only, left axis) vs. scaled position y at the signal front for the TFI model at different h for various signal types. $G(y) = [Ai'(y)]^2 - y Ai(y)^2$ and $H(y)$ are the density and entropy scaling functions for TB fermions [44]. The lines are successively offset by 0.25 in vertical direction.

on site n_0 inside the window, where c^\dagger, c are JW fermion operators (see [62] and Appendix B). This corresponds to a spin flip in z -direction at site n_0 and a domain wall in x -direction between sites $n_0 - 1$ and n_0 . Window movement is triggered by bipartite entanglement entropy, resulting in window velocities consistent with exact maximum velocities (Appendix B). We use a second order Suzuki-Trotter decomposition with a step size of $\tau = 0.002$ and maximum matrix dimension $m_{\text{max}} = 120$ during time evolution. The time evolution inside the CMW (figure 2) shows that boundary effects are indeed removed at both ends of the CMW. In Appendix D we show that results inside the CMW are unperturbed to very high accuracy (about 10^{-8}) at all times.

When the window is not moved (figure 2, inset), the signal is absorbed by both boundaries temporarily, but reflections emerge eventually with both methods. This remains true also for additional models studied in Appendix F, in all cases. We also investigate a pure domain wall (DW) excitation $\prod_{n < n_0} (2\hat{S}_n^z) |\downarrow\rangle$ between sites $n_0 - 1$ and n_0 and a spin flip in x -direction (FlipX) $(2\hat{S}_{n_0}^x) |\downarrow\rangle$ at site n_0 .

3.1.1. Step structure. Despite different global shapes (see Appendix E) for the different excitations, we find that a step structure always develops in $S^x(n,t)$ at the signal front at large times (figure 3), similar to the time evolution from an initial DW state for TB

fermions [41, 42, 44]. The step structure takes much longer to develop for FlipX and DW excitations than for the JW case. The transverse magnetization $S^z(n, t)$ does not show such a step structure.

The step structure is expected to be related to the ballistic nature of propagation at the signal front [36, 37, 44], like for TB fermions, where the steps are now fully understood as individual propagating particles [44]. For the TFI model, in different quench scenarios where two initially separate chains are joined, beginnings of steps have previously been visible in results of [27], but have not been investigated further. We are not aware of other occurrences for the symmetry broken phase. In the paramagnetic phase at large $2h = 10$, TB-like scaling has been observed in [25] for the *transverse* magnetization $S^z(n, t)$ after joining two initially separate chains at different temperatures. No steps occurred for the longitudinal magnetization. Due to their quantum origin these steps appear not to be accessible [44, 63] by semi-classical approaches such as in [13].

We find that the proper quantity to analyze our results is the normalized excess longitudinal magnetization

$$M(n, t) \equiv [S^x(n, t) - S_{\text{GS}}^x] / |2S_{\text{GS}}^x| . \quad (5)$$

Figure 3 shows that at large times this quantity indeed obeys the same scaling behaviour as the particle density of TB fermions [44] at the signal front. For the DW and FlipX cases, there is an additional proportionality factor $C \neq 1$. The asymptotic scaling function $G(y)$ for TB fermions [44] is approached from different directions for different excitations. For DW and FlipX excitations, the exponent α with best data collapse depends on h , whereas for the JW case it is independent of h .

3.1.2. Exact identity. In fact, for the JW excitation we find a surprising much closer identity with TB fermions: The complete time evolution of the normalized excess longitudinal magnetization obeys

$$M(n, t) = N_{\text{TB}}(n, vt) \quad (6)$$

where $v = h$ is the TFI signal velocity (Appendix B.2) and $N_{\text{TB}}(n, vt)$ is the particle density of TB fermions at time vt after a DW excitation (steplike initial density as in [44]). We find this identity to hold up to the numerical precision of our data for all sites n and times t for $h < h_c$, i.e. in the ferromagnetic phase, but for the longitudinal magnetization only.

The steps in $N_{\text{TB}}(n, t)$ have been shown to correspond to individual propagating particles [42, 44] and we note that in the case of the TFI model a similar interpretation in terms of individual quasi-particles can only be given to the scaled excess longitudinal magnetization $M(n, t)$ after a JW excitation in the ferromagnetic phase. Due to the twofold degeneracy of the ground state in this phase the application of a *local* perturbation in the fermion picture generates a topologically non-trivial excitation by creating a domain wall (plus spin flip) in the spin picture, which then decays like a

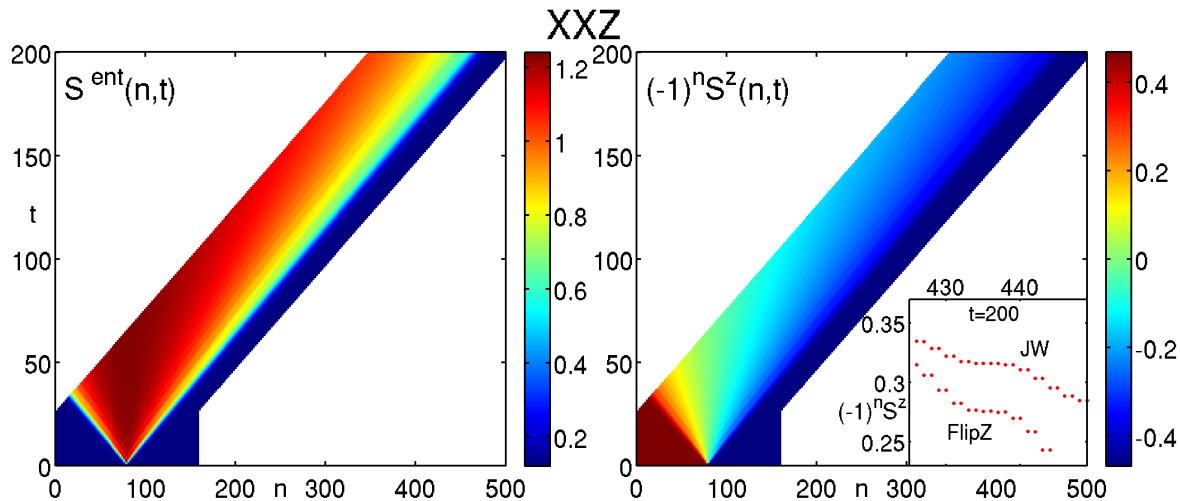


Figure 4. Time evolution of bipartite entanglement entropy $S_{\text{ent}}(n, t)$ and staggered magnetization $\tilde{S}^z(n, t)$ in the XXZ antiferromagnet at $\Delta = -4$ after a JW excitation. We show times up to $t = 200$ in order to keep structures resolvable to the eye, while simulations were performed up to $t = 1000$. *Inset:* Magnification of the signal front at $t = 200$ showing an internal step structure due to pairing.

domain wall of TB fermions with time scale vt . In the paramagnetic phase the same excitation would create a local excitation also in the spin picture, i.e. no domain wall.

Other observables, however, are different between the TFI model and TB fermions. The transverse magnetization $\langle \hat{S}^z \rangle$ is finite in the TFI model (see Appendix B) while the corresponding quantity $\langle c^\dagger + c \rangle$ vanishes for TB fermions. The bipartite entanglement $S_{\text{ent}}(n, t)$ in the TFI model also develops a step structure, but it is at all times smaller than for TB fermions (see Appendix E) and it exhibits different scaling behaviour (see figure 3). This fact only becomes fully apparent at large enough times, which our approach can provide. It would be interesting if the above identity between TB fermions and the TFI model could be understood in more detail analytically.

3.2. XXZ model

Inspired by the above observations in the TFI model in the symmetry broken ferromagnetic phase, we also investigate the XXZ antiferromagnet [19, 20, 21, 22, 23, 28, 29, 30, 31, 32, 33, 34, 35, 36, 37, 38, 39],

$$\hat{H} = - \sum_n (\hat{S}_n^x \hat{S}_{n+1}^x + \hat{S}_n^y \hat{S}_{n+1}^y + \Delta \hat{S}_n^z \hat{S}_{n+1}^z), \quad (7)$$

in the gapped symmetry broken phase for several $\Delta < -1$, where the ground state is also twofold degenerate. We prepare the system in the maximally symmetry broken ground state $|\Downarrow\rangle$ with staggered magnetization $\tilde{S}_{\text{GS}}^z = (-1)^n \langle \hat{S}_n^z \rangle < 0$ using iDMRG and again study the evolution of a JW excitation

$$(c_{n_0}^\dagger + c_{n_0}) |\Downarrow\rangle = \prod_{n < n_0} (-2\hat{S}_n^x)(2\hat{S}_{n_0}^z) |\Downarrow\rangle \quad (8)$$

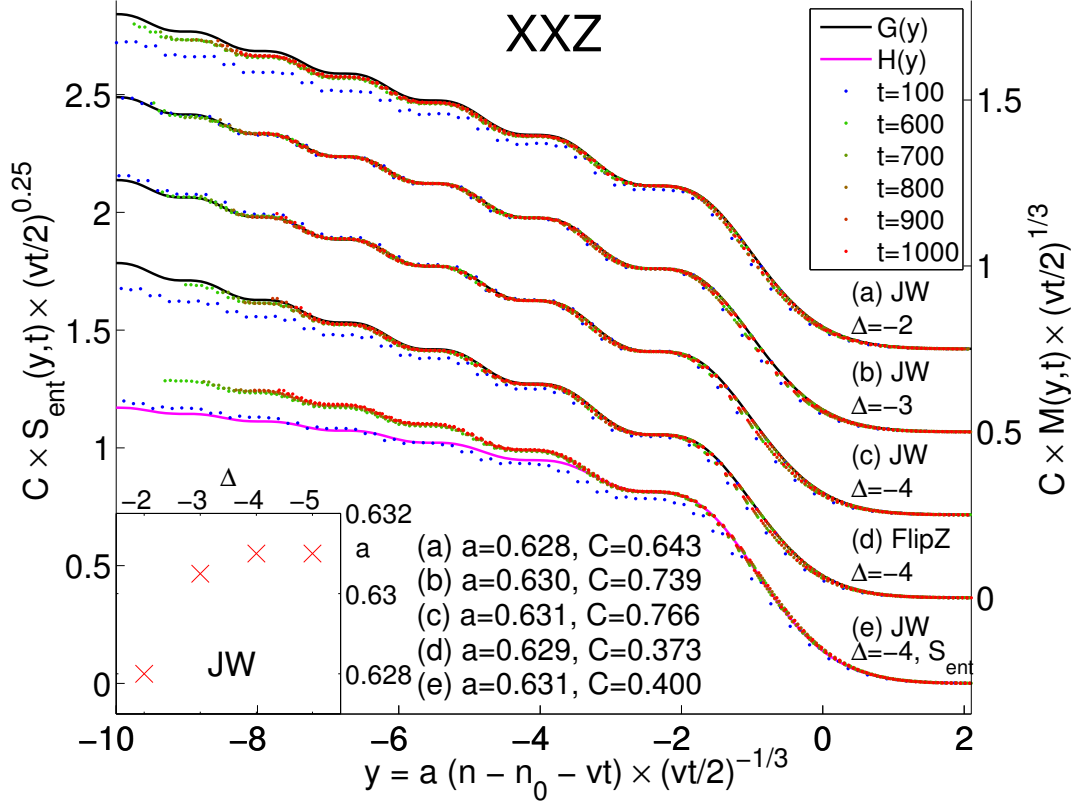


Figure 5. Scaled staggered normalized excess magnetization $M(y,t)$ (right axis) and bipartite entanglement entropy $S_{\text{ent}}(y,t)$ (bottom only, left axis) vs. scaled position y at the signal front for the XXZ model at different Δ for various signal types. $G(y)$ and $H(y)$ are the same scaling functions as in figure 3. The lines are successively offset by 0.25 in vertical direction. *Inset:* Horizontal scaling parameter a as a function of Δ for JW excitations.

at site n_0 inside the window (figure 4).

Notice that due to $S_{\text{GS}}^x = 0$ a JW excitation is locally indistinguishable from a simple domain wall according to the magnetization and that the roles of x and z are interchanged with respect to TFI results. Additionally, we also study a spin flip in z -direction at site n_0 (FlipZ). Window movement is triggered by bipartite entanglement entropy, resulting in window velocities consistent with exact results (see Appendix C). During time evolution we use a second order Suzuki-Trotter decomposition with a step size of $\tau = 0.01$ and maximum matrix dimensions of $m_{\text{max}} = 150$ for $\Delta = -4$, $m_{\text{max}} = 160$ for $\Delta = -3$ and $m_{\text{max}} = 180$ for $\Delta = -2$ with discarded weights of at most $O(10^{-8})$.

The signal front again develops a step structure. To our knowledge this had not been realized before our study, however it was recently confirmed [36, 39] after the preprint version of our study, but not further investigated. We also observe a pairing effect between neighbouring spins, leading to an additional internal step structure, which stems from the spinon like nature of elementary excitations created by the quench (figure 4 inset). Due to the dynamics generated by (7), elementary spinons can only hop by two

lattice sites at a time.

We find that at very large times – which are virtually impossible to access with conventional MPS techniques [28, 34] – the staggered normalized excess magnetization

$$M(n, t) := [\tilde{S}^z(n, t) - \tilde{S}_{\text{GS}}^z] / |2\tilde{S}_{\text{GS}}^z| \quad (9)$$

at the signal front shows the same scaling behaviour as TB fermions, albeit with an additional horizontal scaling constant a , which is parameter dependent and increases with $|\Delta|$ (figure 5 and inset). We therefore again interpret magnetization steps as due to individual propagating quasi-particles, which however show interaction effects by getting squeezed together more and more around the signal front with increasing $|\Delta|$. This behaviour can be explained by the fact that particles repel each other more with increasing interaction, but at the same time they are confined within the light cone dictated by the Lieb-Robinson bound. Since the particle density is much lower around the signal front, more and more particles are pushed towards the signal front and get squeezed together there. Our data however suggests that this effect saturates around $|\Delta| \approx 5$ (see inset of figure 5). It would be very interesting to understand these interaction effects between individual steps in more detail analytically.

The asymptotic scaling function $G(y)$ is approached differently for different Δ , but the scaling exponents appear to be independent of Δ for all quenches investigated. For $M(n, t)$ they are equal to the TB case with value $1/3$, whereas we again find a different effective exponent of $\approx 1/4$ for the bipartite entanglement entropy (figure 5).

4. Conclusions

We have introduced an easy-to-implement method combining finite and infinite system MPS techniques that can follow the propagation of a signal front on an infinite spin chain unimpeded and free from finite size effects for very long simulation times and with very high precision, considerably improved over other approaches. We note that even when the window is not moved, local signals can be simulated on the background of an infinite system, without perturbations emanating from the boundary. In this scenario the signal can be temporarily absorbed by the boundary, though it is always reflected eventually.

Furthermore, the method is not restricted to the evolution of excitations under uniform Hamiltonians. For example, the AKLT model [64] with inhomogeneous bond interactions or 1D quantum systems under exponential or hyperbolic deformation [65, 66] have uniform ground states, whereas the Hamiltonians are not uniform.

To simulate the time evolution of a signal front of width L propagating with velocity v up to some time t , our method requires numerical effort of the order $O(Lt)$, whereas for the same calculation using standard finite size MPS techniques numerical effort would scale as $O(Lt + vt^2)$, i.e. with an additional v -dependent factor which scales quadratically in simulation time. We want to emphasize that additionally, standard finite size MPS techniques would also suffer from finite size effects such as boundary effects or the absence of exact ground state degeneracies in symmetry broken phases.

We have found that for all local quenches investigated in the symmetry broken phases of the TFI and the XXZ model, distinct magnetization plateaus develop at the emerging signal front at very large times, where the scaled excess magnetizations in both models show the same long time limit scaling behaviour as the particle density of TB fermions after an initial domain wall excitation. For TB fermions these plateaus have recently been understood as due to individual propagating particles [44]. Because of their quantum origin these plateaus can not be studied [44, 63] by means of semiclassical approaches such as in [13].

Our method has enabled us to calculate the time evolution of the order parameters of both models around the signal fronts generated by local quenches and investigate their features, which to our knowledge are available neither analytically nor semi-classically. In all cases it is important to reach very large simulation times – which are easily accessible through our approach – in order to reach the proper scaling regimes.

In the XXZ model we have observed an additional internal step structure due to the spinon nature of the involved elementary excitations, as well as parameter dependent interaction effects between individual plateaus in the form of increasing spatial compression of the plateau width close to the signal front. This effect appears to saturate for $|\Delta| \gg 1$. For the TFI model we have additionally found a surprising exact agreement of the normalized excess longitudinal magnetization after a JW excitation with the density of TB fermions after a domain wall excitation. This exact mapping however does not apply to other observables such as e.g. bipartite entanglement.

It would be interesting to understand both the interaction effects between plateaus in the XXZ model and the exact agreement between the TFI model and TB fermions in more detail analytically.

Acknowledgments

We would like to thank Th. Barthel, V. Eisler, F. Maislinger, M.M. Rams, D. Schuricht, U. Schollwöck, and F. Verstraete for valuable discussions. This work was supported by the Austrian Science Fund (FWF): F4104 SFB ViCoM and by the EP - SRC under grant EP/I032487/1. T.N. acknowledges the support of Grant-in-Aid for Scientific Research (C) No. 22540388.

Appendix A. CMW Time Evolution and Boundary Update Methods

In this appendix we illustrate one time evolution step for the entire system when following a right moving signal. We describe the procedure in the following order. We first evolve the part of the system contained within the CMW (Appendix A.2) before updating the right part using Method I (Appendix A.3) and updating the left part using the more involved Method II (Appendix A.4 and Appendix A.5). Note that this is the setup used in the main text, however in principle any of the two methods can be used at any boundary. A detailed assessment of different setups is given in Appendix D. We also describe the process of moving the CMW along with a propagating signal (Appendix A.6). A short sketch of both boundary update methods, illustrating their advantages and restrictions, along with a motivation of the above choice is given in the main text.

Appendix A.1. System Initialization

In the main text in particular we use a setup dividing the system into a semi-infinite, initially translation invariant left part, a finite-size CMW (inside of which a signal will be created) and a semi-infinite, at all times translation invariant right part. We initialize the system by first determining a uniform MPS representation of the respective model's ground state on an infinite chain using iDMRG [6, 48]. We then set all MPS matrices inside the CMW (matrices A^{σ_j} and B^{σ_j}), the semi-infinite right part (matrices R_A^σ and R_B^σ forming this part's two-site unit cell) and the semi-infinite left part (*all* matrices L^{σ_j}) to this uniform MPS ground state representation after appropriate (left or right) orthonormalization [5, 48], i.e. we initialize the entire system to be in the infinite system's translation invariant ground state. Subsequently we locally excite the system out of its ground state to generate several different kinds of local signals by applying suitable operators to one or more MPS matrices inside the CMW.

For other purposes the generalization to different initial conditions is straight forward.

Appendix A.2. Time Evolution within the CMW (CMW Update)

Without loss of generality we consider a CMW with an even number of sites and first order even-odd Suzuki-Trotter decomposition [58] with local operators $\hat{u}_{j,j+1}(\tau) = e^{-i\tau\hat{h}_{j,j+1}}$ and finite time steps τ . The generalization to higher order Suzuki-Trotter decompositions and windows containing an odd number of sites is straight forward. All simulations in this work have been performed using second order Suzuki-Trotter decomposition and windows with an even number of sites.

For one time step inside the CMW we use tDMRG [8] and apply $\hat{u}_{j,j+1}(\tau) = e^{-i\tau\hat{h}_{j,j+1}}$ to the bonds from $(\ell+1, \ell+2)$ until $(r-1, r)$ and update matrices A^{s_j} and B^{s_j} contained within the CMW. The junction bonds $(\ell, \ell+1)$ and $(r, r+1)$ at the left and right boundary of the CMW are updated separately.

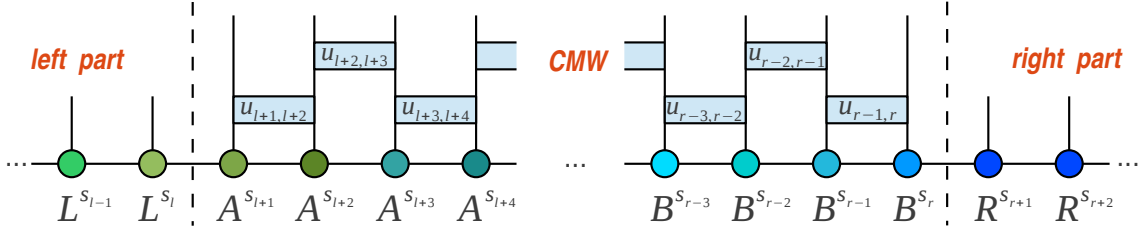


Figure A1. One time step of the CMW update in the case of first order Suzuki-Trotter decomposition and a CMW with an even number of sites.

We first update all *odd* bonds $\{\dots, (r-3, r-2), (r-1, r)\}$ and then all *even* bonds $\{\dots, (r-4, r-3), (r-2, r-1)\}$. The junction bonds $(\ell, \ell+1)$ and $(r, r+1)$ are thus defined to be even bonds (see figure A1). By choosing this order we preserve the structure of the Suzuki-Trotter decomposition of the CMW and the right part, when Method I is used to update the right boundary.

At this stage all even and odd bonds have been updated, except for the junction bonds $(\ell, \ell+1)$ and $(r, r+1)$, i.e. the boundary matrices $A^{s_{\ell+1}}$ and B^{s_r} are not yet fully updated.

Note that an implementation of this update using Time Evolving Block Decimation (TEBD [7]) is equivalent. For a graphical representation see figure A1.

Appendix A.3. Method I (Uniform Update).

We use this easy to implement procedure for the right boundary. Due to the assumed translation invariance over a 2-site unit cell, this part can be described by two right-orthogonal matrices $R_A^{s_j}$ and $R_B^{s_j}$, such that the wavefunction in MPS representation around the right boundary reads

$$\dots B^{s_{r-1}} B^{s_r} R_A^{s_{r+1}} R_B^{s_{r+2}} R_A^{s_{r+3}} R_B^{s_{r+4}} \dots \quad (\text{A.1})$$

The evolution of the matrices $R_A^{s_j}$ and $R_B^{s_j}$ is performed by iTEBD (or variations thereof) using local operators $\hat{u}^A(\tau)$ and $\hat{u}^B(\tau)$ [47, 67], where $\hat{u}^A(\tau)$ acts on *odd* bonds and $\hat{u}^B(\tau)$ acts on *even* bonds.

In a first step, we apply an *odd* bond iTEBD update in the right part to get

$$R_{A\circ}^{s_A} R_{B\circ}^{s_B} = \sum_{s'_A s'_B} u(\tau)_{(s_A s_B)(s'_A s'_B)}^A R_A^{s'_A} R_B^{s'_B}, \quad (\text{A.2})$$

where \circ denotes matrices having received an odd bond update. Here the decomposition of the result of the right hand side of (A.2) is implicitly assumed. It can be done by an SVD either involving a division by Schmidt values following [47] or avoiding the division by Schmidt values by using the approach of [67].

The wavefunction at this point reads

$$\dots B_{\bullet}^{s_{r-2}} B_{\bullet}^{s_{r-1}} B_{\circ}^{s_r} R_{A\circ}^{s_{r+1}} R_{B\circ}^{s_{r+2}} \dots, \quad (\text{A.3})$$

where \bullet denotes matrices having received both odd and even updates.

- (i) Apply odd iTEBD update to get $R_{A\circ}^{s_A}, R_{B\circ}^{s_B}$.
- (ii) Use $R_{A\circ}^{s_A}$ to form $\Phi_{\circ\circ}^{s_r s_{r+1}} = B_{\circ}^{s_r} R_{A\circ}^{s_{r+1}}$
- (iii) Apply $\hat{u}_{r,r+1}$ to get $\Phi_{\bullet\bullet}^{s_r s_{r+1}}$.
- (iv) Apply even iTEBD update to get $R_{B\bullet}^{s_B}, R_{A\bullet}^{s_A}$.
- (v) Use $R_{A\bullet}^{s_A}$ to obtain $B_{\bullet}^{s_r} = \sum_{s_{r+1}} \Phi_{\bullet\bullet}^{s_r s_{r+1}} R_{A\bullet}^{s_{r+1}\dagger}$.

Table A1. Algorithm for *Method I* updating the right boundary of the CMW. For a graphical representation see figure A2.

Special attention has to be paid to the operation of $\hat{u}_{r,r+1}(\tau)$ at the junction bond in order to update $B_{\circ}^{s_r}$. For this we form $\Phi_{\circ\circ}^{s_r s_{r+1}} := B_{\circ}^{s_r} R_{A\circ}^{s_{r+1}}$ and act with $\hat{u}_{r,r+1}$ to get $\Phi_{\bullet\bullet}^{s_r s_{r+1}}$. In parallel we perform an *even* bond iTEBD update in the right part to get

$$R_{B\bullet}^{s_B} R_{A\bullet}^{s_A} = \sum_{s'_A s'_B} u(\tau)_{(s_B s_A)(s'_B s'_A)}^B R_{B\circ}^{s'_B} R_{A\circ}^{s'_A}. \quad (\text{A.4})$$

where again the decomposition of the result of the right side is implicitly assumed.

All bonds have now been updated. Since there is negligible influence of the signal around the right boundary by construction, the state of the right part should be the same as for a time evolved uniform system without signal up to high precision, i.e. we can also assume $\Phi_{\bullet\bullet}^{s_r s_{r+1}} = B_{\bullet}^{s_r} R_{A\bullet}^{s_{r+1}}$, where both $B_{\bullet}^{s_r}$ and $R_{A\bullet}^{s_{r+1}}$ are right-orthogonal and $R_{A\bullet}^{s_{r+1}}$ is obtained from (A.4). We extract $B_{\bullet}^{s_r}$ from $\Phi_{\bullet\bullet}^{s_r s_{r+1}}$ by exploiting the right-orthogonality of $R_{A\bullet}^{s_{r+1}}$:

$$B_{\bullet}^{s_r} = \sum_{s_{r+1}} \Phi_{\bullet\bullet}^{s_r s_{r+1}} R_{A\bullet}^{s_{r+1}\dagger}. \quad (\text{A.5})$$

The wavefunction in MPS form is now completely updated around the right boundary and reads

$$\dots B_{\bullet}^{s_{r-2}} B_{\bullet}^{s_{r-1}} B_{\bullet}^{s_r} R_{A\bullet}^{s_{r+1}} R_{B\bullet}^{s_{r+2}} \dots \quad (\text{A.6})$$

We note that in general, the decomposition $\Phi_{\bullet\bullet}^{s_r s_{r+1}} = \tilde{B}_{\bullet}^{s_r} \tilde{R}_{\bullet}^{s_{r+1}}$ into right-orthogonal matrices is not unique, but involves a gauge freedom $\tilde{B}_{\bullet}^{s_r} \tilde{R}_{\bullet}^{s_{r+1}} = B_{\bullet}^{s_r} x^{-1} R_{A\bullet}^{s_{r+1}}$ with x a unitary matrix (Exploiting right orthogonality of both $\tilde{R}_{\bullet}^{s_{r+1}}$ and $R_{A\bullet}^{s_{r+1}}$ we have $\mathbb{1} = \sum_s \tilde{R}_{\bullet}^{s_{r+1}} \tilde{R}_{\bullet}^{s_{r+1}\dagger} = x \sum_s R_{A\bullet}^{s_{r+1}} R_{A\bullet}^{s_{r+1}\dagger} x^\dagger = x x^\dagger$. Since x is square this also means $x^\dagger x = \mathbb{1}$ and thus x is unitary.).

If the decomposition $\Phi_{\bullet\bullet}^{s_r s_{r+1}} = \tilde{B}_{\bullet}^{s_r} \tilde{R}_{\bullet}^{s_{r+1}}$ was carried out in the standard TEBD/tDMRG way (i.e. by means of an SVD), then a different gauge $\tilde{R}_{\bullet}^{s_{r+1}} \neq R_{A\bullet}^{s_{r+1}}$ and thus $\tilde{B}_{\bullet}^{s_r} \neq B_{\bullet}^{s_r}$ would result in general, since $\tilde{R}_{\bullet}^{s_{r+1}}$ was produced algorithmically in a different way than $R_{A\bullet}^{s_{r+1}}$. In that case, i.e. if $\tilde{B}_{\bullet}^{s_r}$ was used instead of $B_{\bullet}^{s_r}$, incompatible basis sets would meet at the junction bond, which would result in perturbations spreading from the boundary. By use of (A.5) we ensure that the correct gauge is chosen automatically.

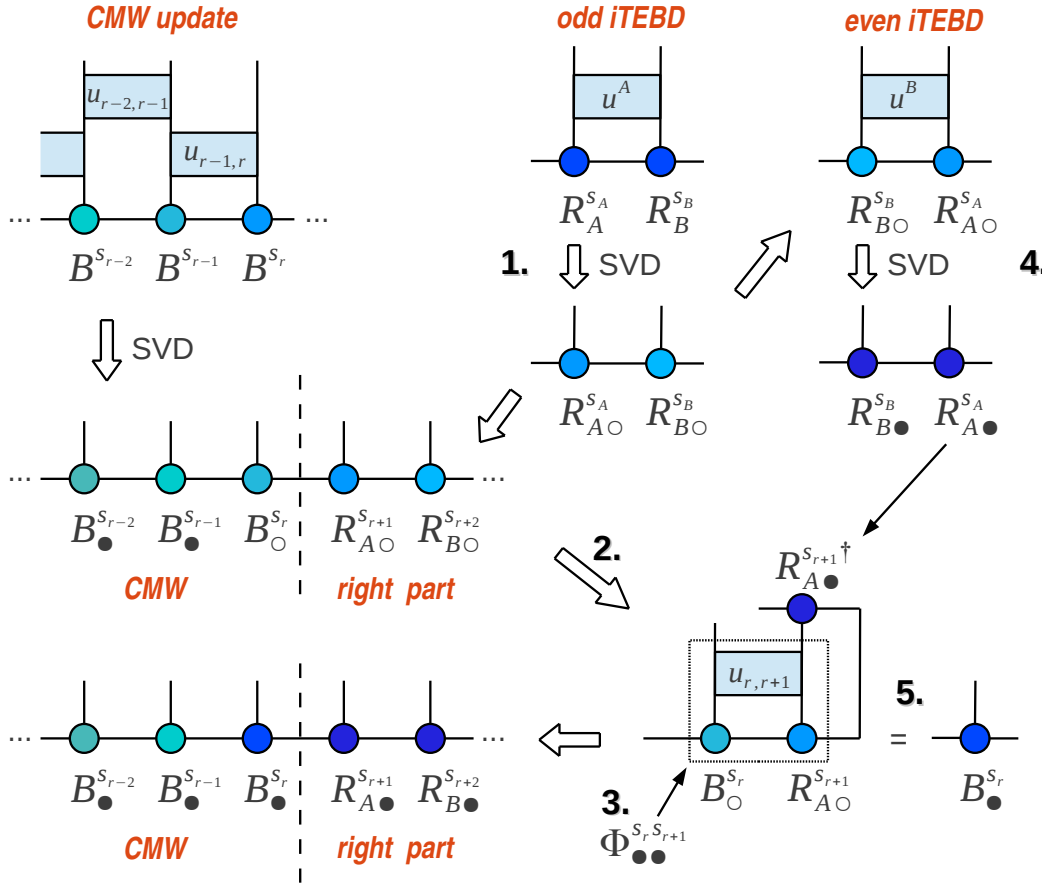


Figure A2. Graphical representation for updating the right boundary of the CMW with Method I according to the steps in table A1.

This concludes one time step for the right part and right boundary. For an algorithmic summary see table A1, for a detailed graphical representation see figure A2.

The procedure can also be easily translated to the left boundary exploiting left orthogonality, where translation invariance of the left-orthogonal matrices L^{s_j} is then required.

Method I is also applicable when H_R is time dependent, e.g. in case of a global quench.

Appendix A.4. Method II (Renormalized Update)

We use this procedure for the left boundary. For this Method we follow a similar approach as introduced by Cazalilla and Marston [59] (Method II is similar to the algorithm introduced in [50], where preprints of [50] and of the present paper appeared at the same time), such that matrices L^{s_j} in the left part remain unchanged at all times during time evolution.

The effect of the left part is encoded in a renormalized formulation of $\hat{H}_{\leftarrow, \ell+1} :=$

- (i) Perform only once for each CMW position:
- (a) Determine renormalized expression $H_{\triangleleft, \ell+1}^{\text{eff}}$ of $\hat{H}_{\triangleleft, \ell+1}$, formulated in block-spin basis $\{|a_\ell s_{\ell+1}\rangle\}$.
 - (b) Calculate $U(\tau)_{\triangleleft, \ell+1}^{\text{eff}} = \exp(-i\tau H_{\triangleleft, \ell+1}^{\text{eff}})$.
- (ii) Update $A_{\circ}^{s'_{\ell+1}}$ using $U_{\triangleleft, \ell+1}^{\text{eff}}$ in each time step to get $A_{\bullet}^{s_{\ell+1}} = \sum_{s'_{\ell+1}} U(\tau)_{\triangleleft, \ell+1}^{\text{eff}, s_{\ell+1} s'_{\ell+1}} A_{\circ}^{s'_{\ell+1}}$.

Table A2. Algorithm for *Method II* updating the left boundary of the CMW. For a graphical representation see figure A4.

$\hat{H}_L + \hat{h}_{\ell, \ell+1}$, which is exactly the renormalized Hamiltonian used in standard DMRG formulations (see e.g. [4, 5]). All changes in the left part are then solely encoded in an update of the boundary matrix $A^{s_{\ell+1}}$. Note that for this method the matrices L^{s_j} in the left part need not be translation invariant.

Since matrices L^{s_j} are not changed during this update, we rewrite the wavefunction in MPS form after the CMW update in terms of the auxiliary basis states $|a_\ell\rangle = \sum_{s_j \leq \ell} (\dots L^{s_{\ell-1}} L^{s_\ell})_{a_\ell} |\dots s_{\ell-1} s_\ell\rangle$ connecting L^{s_ℓ} and $A^{s_{\ell+1}}$:

$$\Psi(a_\ell | s_{\ell+1}^\circ s_{\ell+2}^\bullet \dots; t) = (A_{\circ}^{s_{\ell+1}} A_{\bullet}^{s_{\ell+2}} \dots)_{a_\ell}, \quad (\text{A.7})$$

where a_ℓ is the left index of matrix $A_{\circ}^{s_{\ell+1}}$. The right hand side of (A.7) is formally just the semi-infinite product of all matrices to the right of site ℓ . The overall state vector after the CMW update can thus also be written

$$|\Psi(t)\rangle = \sum_{a_\ell} \sum_{s_{\ell+1} \dots} \Psi(a_\ell | s_{\ell+1}^\circ s_{\ell+2}^\bullet \dots; t) |a_\ell\rangle |s_{\ell+1} \dots\rangle. \quad (\text{A.8})$$

Here \bullet and \circ again mark sites which have received a complete and incomplete update respectively. Notice that in Method II the basis $\{|a_\ell\rangle\}$ will remain unchanged at all times. For a graphical representation of (A.7) see figure A3(a).

We now need a renormalized representation $H_{\triangleleft, \ell+1}^{\text{eff}}$ of $\hat{H}_{\triangleleft, \ell+1}$ formulated in the block-spin basis $\{|a_\ell s_{\ell+1}\rangle\}$. A possible method to calculate $H_{\triangleleft, \ell+1}^{\text{eff}}$ is outlined in Appendix A.5. Once we have such a renormalized expression we can determine the renormalized time evolution operator for the left part

$$U(\tau)_{\triangleleft, \ell+1}^{\text{eff}} := \exp(-i\tau H_{\triangleleft, \ell+1}^{\text{eff}}), \quad (\text{A.9})$$

where we use the same small time step τ as for the Suzuki-Trotter updates. This time evolution operator is then used to update $\Psi(a_\ell | s_{\ell+1}^\circ s_{\ell+2}^\bullet \dots; t)$. However, as it is a unitary operator defined in the block-spin basis $\{|a_\ell s_{\ell+1}\rangle\}$, it only updates $A_{\circ}^{s_{\ell+1}}$ and we get

$$A_{\bullet}^{s_{\ell+1}} = \sum_{s'_{\ell+1}} U(\tau)_{\triangleleft, \ell+1}^{\text{eff}, s_{\ell+1} s'_{\ell+1}} A_{\circ}^{s'_{\ell+1}}. \quad (\text{A.10})$$

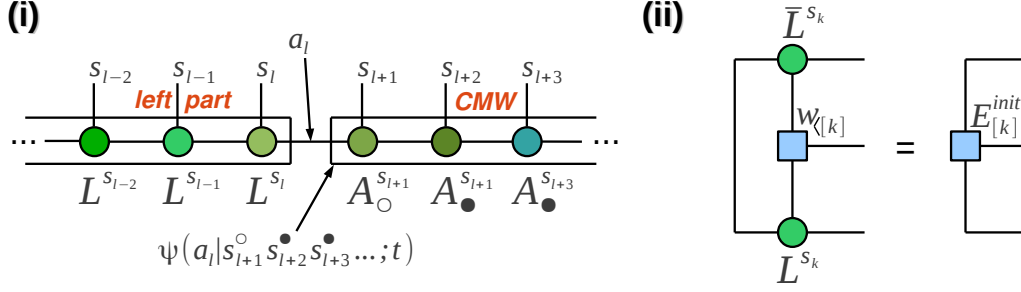


Figure A3. (i) Graphical Representations of the definition of $\Psi(a_\ell | s_{\ell+1}^\circ, s_{\ell+2}^\bullet, \dots; t)$ in (A.7). Note that the matrices L^{s_j} within the left part and the basis $\{|a_\ell\rangle\}$ remain unchanged during the simulation for Method II. (ii) Graphical representation of the construction of the initial element $E_{[k]}^{\text{init}}$ defined in (A.19) to approximate the semi-infinite product $E_{[\ell]}$.

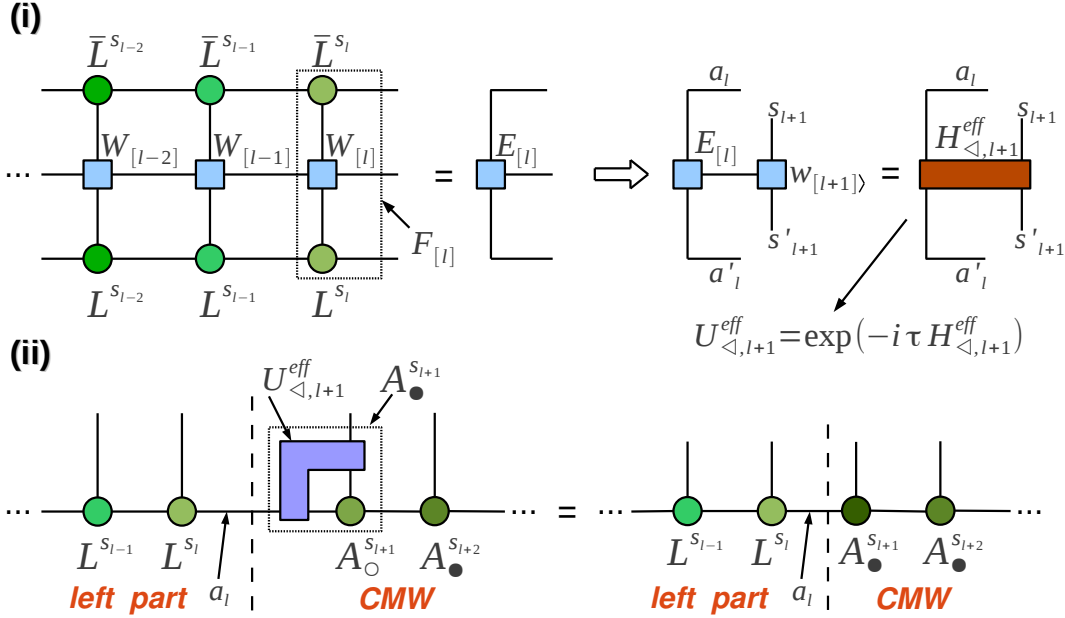


Figure A4. Graphical representation for updating the left boundary of the CMW with Method II with the steps listed in table A2. (i) Constructing the renormalized Hamiltonian $H_{\langle, l+1}^{\text{eff}}$ as outlined in Appendix A.5 and there defined in (A.17). (ii) Using the renormalized time evolution operator $U(\tau)_{\langle, l+1}^{\text{eff}}$ as defined in (A.9) to update the left boundary matrix $A^{s_{\ell+1}}$ according to (A.10).

This concludes one time step for the left boundary. Notice that the matrices in the left part are *not* updated as all change in the left part are compressed into the boundary matrix $A^{s_{\ell+1}}$ with constant basis $\{|a_\ell\rangle\}$. In this sense the update is non-adaptive.

Notice also that $U_{\langle, l+1}^{\text{eff}}$ breaks the structure of the even-odd Suzuki-Trotter decomposition in the left part. This introduces an additional error, which is of the same order as the Suzuki-Trotter error and can in principle be made arbitrarily small by using higher order Suzuki-Trotter decompositions and smaller time steps τ at the

cost of increased computational time. The effect of this additional error is investigated in detail in Appendix D. It could be avoided by using the renormalized imaginary-time transfer matrix, as used in finite temperature DMRG [68], to update $A_\circ^{s_{\ell+1}}$. For an algorithmic summary see table A2, for a graphical representation of this update see figure A4.

Appendix A.5. Renormalized Hamiltonian for Method II

For determining $H_{\triangleleft, \ell+1}^{\text{eff}}$ used in Method II, we first assume a left part that is semi-infinite. Consider \hat{H} in MPO form [69, 70, 71, 72, 73]

$$\hat{H} = \sum_{\mathbf{s}} \prod_{j=-\infty}^{\infty} W_{[j]}^{s_j s'_j} |\mathbf{s}\rangle \langle \mathbf{s}'|, \quad (\text{A.11})$$

where $W_{[j]}^{s_j s'_j}$ are matrices of some dimension $d_W \times d_W$ containing operator elements $O^{s_j s'_j}$. This decomposition can also be written in operator form, where we define $\hat{W}_{[j]} := \sum_{s_j s'_j} W_{[j]}^{s_j s'_j} |s_j\rangle \langle s'_j|$ as $d_W \times d_W$ matrices containing operators. We can then simply write $\hat{H} = \prod_{j=-\infty}^{\infty} \hat{W}_{[j]}$. For finite size (or semi-infinite) operators, this product of MPO matrices is terminated by d_W -dimensional operator-valued boundary vectors $\hat{w}_{\langle [j]}$ and (or) $\hat{w}_{[j]\rangle}$.

An example for an MPO decomposition for the Transverse Field Ising (TFI) Hamiltonian $\hat{H}_{\text{TFI}} = -\sum_j \hat{S}_j^x \hat{S}_{j+1}^x - h \sum_j \hat{S}_j^z$ is given by

$$\hat{W}_{[j]} = \begin{bmatrix} \hat{\mathbf{1}}_j & 0 & 0 \\ -\hat{S}_j^x & 0 & 0 \\ -h\hat{S}_j^z & \hat{S}_j^x & \hat{\mathbf{1}}_j \end{bmatrix} \quad (\text{A.12})$$

$$\hat{w}_{\langle [j]} = \begin{bmatrix} -h\hat{S}_j^z & \hat{S}_j^x & \hat{\mathbf{1}}_j \end{bmatrix} \quad \hat{w}_{[j]\rangle} = \begin{bmatrix} \hat{\mathbf{1}}_j & -\hat{S}_j^x & -h\hat{S}_j^z \end{bmatrix}^T. \quad (\text{A.13})$$

For the TFI Hamiltonian we thus have $d_W = 3$.

We can express $\hat{H}_{\triangleleft, \ell+1}$ in terms of an MPO as

$$\hat{H}_{\triangleleft, \ell+1} = \dots \hat{W}_{[\ell-1]} \hat{W}_{[\ell]} \hat{w}_{[\ell+1]\rangle}, \quad (\text{A.14})$$

where we have terminated the semi-infinite product of MPO matrices with the boundary vector $\hat{w}_{[\ell+1]\rangle}$.

In order to get $H_{\triangleleft, \ell+1}^{\text{eff}}$ we use matrices L^{s_j} to renormalize $\hat{H}_{\triangleleft, \ell+1}$. For this, consider the $d_W \times d_W$ dimensional *MPO transfer matrix* defined as

$$F_{[j]}^{b_{j-1} b_j} := \sum_{s_j s'_j} W_{[j], b_{j-1} b_j}^{s_j s'_j} \bar{L}^{s_j} \otimes L^{s'_j}, \quad (\text{A.15})$$

containing $m^2 \times m^2$ matrices, where m is the matrix dimension of the MPS matrices L^{s_j} and \bar{L}^{s_j} denotes the complex conjugate of L^{s_j} .

$H_{\triangleleft, \ell+1}^{\text{eff}}$ can then be written as

$$H_{\triangleleft, \ell+1}^{\text{eff}, s_{\ell+1} s'_{\ell+1}} = \sum_{b_{\ell}=1}^{d_W} \left(\prod_{j \leq \ell} F_{[j]} \right)_{b_{\ell}} w_{[\ell+1], b_{\ell}}^{s_{\ell+1} s'_{\ell+1}} \quad (\text{A.16})$$

$$= \sum_{b_{\ell}=1}^{d_W} E_{[\ell]}^{b_{\ell}} w_{[\ell+1], b_{\ell}}^{s_{\ell+1} s'_{\ell+1}}, \quad (\text{A.17})$$

where we have defined the semi-infinite product

$$E_{[\ell]}^{b_{\ell}} := \left(\prod_{j \leq \ell} F_{[j]} \right)_{b_{\ell}}. \quad (\text{A.18})$$

$H_{\triangleleft, \ell+1}^{\text{eff}, s_{\ell+1} s'_{\ell+1}}$ is then a set of $m \times m$ matrices labelled by $s_{\ell+1}$ and $s'_{\ell+1}$ and $E_{[\ell]}$ can be understood as a d_W -dimensional vector containing $m \times m$ matrices. For a graphical representation of these steps see figure A4(1). Note that the vector element $E_{[j]}^1$ accumulates the renormalized Hamiltonian containing all sites $k \leq j$ (see e.g. [70]).

To determine (A.17) we need a way to calculate the semi-infinite matrix product $E_{[\ell]}$. For the moment we consider the case where both \hat{H}_L and the matrices L^{s_j} are translation invariant. In this case $F_{[j]}$ is also translation invariant and $E_{[\ell]}$ can be calculated by e.g. finding the dominant left eigenvector of $F_{[j]}$ as explained in [73].

However here we follow an approximate but sufficiently accurate approach for calculating $E_{[\ell]}$, which is inspired by standard DMRG formulations. For this we relax the condition of semi-infinity for the left Hamiltonian $\hat{H}_{\triangleleft, \ell+1}$ and approximate it with a finite size Hamiltonian, which we increase in size until we get a converged result. The finite size version of $\hat{H}_{\triangleleft, \ell+1}$ in MPO form is thus contracted also on the left side by $\hat{w}_{\langle [k]}$ for some $k \ll \ell$. We first compute an initial $E_{[k]}$ as

$$E_{[k], b_k}^{\text{init}} = \sum_{s_k s'_k} w_{\langle [k], b_k}^{s_k s'_k} L^{s_k \dagger} L^{s'_k}, \quad (\text{A.19})$$

exploiting the left-orthogonality of the matrices L^{s_j} . For a graphical representation see figure A3(b).

We can now iteratively calculate $E_{[j+1]} = E_{[j]} F_{[j+1]}$ many times until this process has converged. As a convergence criterion we can use e.g. the ground state energy per site of the renormalized Hamiltonian which is accumulated in $E_{[j]}^1$. Using the converged result as an approximation for $E_{[\ell]}$ we can then easily determine $H_{\triangleleft, \ell+1}^{\text{eff}}$ from (A.17).

In the case where MPS matrices L^{s_j} and/or MPOs $W_{[j]}^{s_j s'_j}$ are site dependent for some sites $k \leq j \leq \ell$, we can first calculate $E_{[k]}$ up to site k approximately as described above and then calculate the finite product

$$E_{[\ell]} = E_{[k]}^{\text{init}} \prod_{j=k+1}^{\ell} F_{[j]}. \quad (\text{A.20})$$

Notice that we can in principle even define the left part to be finite altogether, with site dependent matrices $L^{s_j \leq \ell}$ and/or site dependent MPOs $W_{[j]}^{s_j s'_j}$, such that $E_{[\ell]} = \prod_{j=1}^{\ell} F_{[j]}$

is also a finite product. In this case one would have to specify left boundary conditions. In our simulations we do not consider this case.

If Method II is used at the right boundary, we use the uniform matrices R^{s_j} to construct a renormalized expression for $\hat{H}_{r,\triangleright} := \hat{h}_{r,r+1} + \hat{H}_R = \sum_{j=r}^{\infty} \hat{h}_{j,j+1}$.

Generally the computational effort for calculating $H_{\triangleleft,\ell+1}^{\text{eff}}$ is dictated by the computational effort for calculating $E_{[\ell]}$. In case of a translation invariant left part, its calculation is very similar to the *renormalization* steps of an iDMRG simulation [6, 48] (no eigenvalue/SVD steps). The number of renormalization steps is dependent on the effective correlation length induced by the uniform MPS matrices L^{s_j} .

In practice it takes about 75 renormalization steps for the TFI model at $h = 0.45$ ($m_0 = 30$) and about 100 steps for the XXZ model at $J_z = -2$ ($m_0 = 88$) for convergence in energy up to an accuracy of 10^{-15} , where m_0 is the bond dimension of the ground state MPS representation. The overall computational effort here is comparable to a few time evolution steps within the CMW.

Appendix A.6. Window Movement

We describe the window movement by a single site. For a shift by a 2-site unit cell, the same procedure as for a single site is applied twice.

If no boundary update is used at the left boundary, the matrix $A^{s_{\ell+1}}$ is discarded. If Method II is used, we incorporate $A^{s_{\ell+1}}$ into the left part by using it to calculate a renormalized expression for $\hat{H}_{\triangleleft,\ell+2} := \hat{H}_{\triangleleft,\ell+1} + \hat{h}_{\ell+1,\ell+2}$. More precisely, we construct $F_{[\ell+1]}$ as defined in (A.15) using $A^{s_{\ell+1}}$

$$F_{[\ell+1]}^{b_{\ell}b_{\ell+1}} := \sum_{s_{\ell+1}s'_{\ell+1}} W_{[\ell+1],b_{\ell}b_{\ell+1}}^{s_{\ell+1}s'_{\ell+1}} \bar{A}^{s_{\ell+1}} \otimes A^{s'_{\ell+1}}. \quad (\text{A.21})$$

With $E_{[\ell]}$ from earlier calculations we can then construct $E_{[\ell+1]} = E_{[\ell]}F_{[\ell+1]}$, calculate $H_{\triangleleft,\ell+2}^{\text{eff}}$ as defined in (A.17) and determine $U(\tau)_{\triangleleft,\ell+2}^{\text{eff}} = \exp(-i\tau H_{\triangleleft,\ell+2}^{\text{eff}})$.

At the right boundary we introduce $R_A^{s_{r+1}}$ as a new rightmost matrix $B^{s_{r+1}}$.

After the window has been moved by a single site according to these steps, we redefine $\ell \leftarrow \ell + 1$, $r \leftarrow r + 1$ (and we exchange labels $A \leftrightarrow B$ in the case of iTEBD).

Notice that for the left boundary the dimension of the block basis $\{|a_{\ell}\rangle\}$ can grow with successive window shifts. An impinging signal can therefore be partly absorbed such that immediate perturbations are considerably suppressed (see also Appendix F).

We trigger the window shift when the relative change of the bipartite entanglement entropy at some site sufficiently far away from the right boundary rises above a certain threshold. The margin between this site and the right boundary should be large in comparison to the correlation length of the initial state such that the exponentially suppressed correlations reaching beyond the Lieb-Robinson light cone [54] are negligible. For all simulations in the main text we use a margin of 24 sites and a threshold of 1%. If known beforehand, the window can also be moved directly with v_{max} .

Appendix B. Analytic Results for the TFI Model

In this appendix, we collect some known results and we derive an exact expression for the transverse magnetization in the TFI model after a Jordan-Wigner excitation.

Appendix B.1. Diagonalization of the Hamiltonian

The TFI model

$$\hat{H}_{TFI} = - \sum_j \hat{S}_j^x \hat{S}_{j+1}^x - h \sum_j \hat{S}_j^z \quad (\text{B.1})$$

can be solved exactly [60, 61] by first transforming to spinless fermionic operators c_j^\dagger, c_j via a Jordan-Wigner (JW) transformation [62]

$$\hat{S}_j^+ = \prod_{n<j} (1 - 2c_n^\dagger c_n) c_j^\dagger, \quad \hat{S}_j^- = \prod_{n<j} (1 - 2c_n^\dagger c_n) c_j, \quad (\text{B.2})$$

where \hat{S}_j^+ and \hat{S}_j^- are the spin raising and lowering operators. With $\hat{S}_j^x = \frac{1}{2} (\hat{S}_j^+ + \hat{S}_j^-)$ and $\hat{S}_j^z = \hat{S}_j^+ \hat{S}_j^- - \frac{1}{2}$ the Hamiltonian becomes

$$\hat{H}_{TFI} = -\frac{1}{4} \sum_j (c_j^\dagger - c_j) (c_{j+1}^\dagger + c_{j+1}) - h \sum_j \left(c_j^\dagger c_j - \frac{1}{2} \right). \quad (\text{B.3})$$

Here we have already taken the thermodynamic limit while considering periodic boundary conditions (A boundary term arising from the JW transformation and periodic boundary conditions is neglected as it is of the order $O(1/L)$ where L is the system size).

A subsequent Bogoliubov transformation [74] to fermionic operators η_k, η_k^\dagger in momentum space

$$c_j = \frac{1}{\sqrt{2\pi}} \int_{-\pi}^{\pi} dk e^{ikj} (a_k \eta_k - ib_k \eta_{-k}^\dagger) \quad (\text{B.4})$$

then diagonalizes the Hamiltonian. The coefficients a_k and b_k are real and satisfy

$$a_{-k} = a_k, \quad b_{-k} = -b_k, \quad a_k^2 + b_k^2 = 1 \quad (\text{B.5})$$

and can be determined as

$$a_k = \frac{\varepsilon_k - \frac{1}{2} \cos(k) - h}{\sqrt{2\varepsilon_k (\varepsilon_k - \frac{1}{2} \cos(k) - h)}} \quad (\text{B.6})$$

$$b_k = -\frac{\frac{1}{2} \sin(k)}{\sqrt{2\varepsilon_k (\varepsilon_k - \frac{1}{2} \cos(k) - h)}} \quad (\text{B.7})$$

$$\varepsilon_k = \sqrt{\frac{1}{4} + h \cos(k) + h^2}. \quad (\text{B.8})$$

The Hamiltonian then reads

$$\hat{H}_{TFI} = \frac{1}{2\pi} \int_{-\pi}^{\pi} dk \varepsilon_k \left(\eta_k^\dagger \eta_k - \frac{1}{2} \right) \quad (\text{B.9})$$

and the ground state corresponds to the vacuum state $|0\rangle$ in terms of the fermionic operators η_k and η_k^\dagger .

Appendix B.2. Signal Velocity in the TFI model

The propagation of a signal induced on top of the ground state $|0\rangle$ of the TFI model can be understood as the excitation and propagation of a superposition of non-interacting particles with momenta k and corresponding energies ε_k created by η_k^\dagger . In this picture, the maximum velocity v_{\max} of the signal can be exactly calculated as the maximum of the group velocity

$$v_k := \frac{d\varepsilon_k}{dk} = \frac{h \sin(k)}{2 \varepsilon_k}. \quad (\text{B.10})$$

A short calculation shows that v_k takes its extrema at $\cos(k) = 2h$ and $\cos(k) = \frac{1}{2h}$, which gives

$$v_{\max} = \begin{cases} h & , \quad h \leq h_{\text{crit}} \\ h_{\text{crit}} & , \quad h \geq h_{\text{crit}} \end{cases} \quad (\text{B.11})$$

where $h_{\text{crit}} = \frac{1}{2}$.

Appendix B.3. Analytic Results for a JW Excitation

Consider a Jordan-Wigner (JW) excitation at site ℓ on top of the thermodynamic limit ground state $|0\rangle$, defined as

$$|\psi\rangle_\ell = (c_\ell^\dagger + c_\ell) |0\rangle \quad (\text{B.12})$$

$$= \frac{1}{\sqrt{2\pi}} \int_{-\pi}^{\pi} dk e^{-ik\ell} (a_k + ib_k) \eta_k^\dagger |0\rangle. \quad (\text{B.13})$$

Using the results from the previous sections for the TFI model, the time evolution of the magnetization in z after such an excitation

$$\langle \hat{S}^z(n, t) \rangle_\ell = \langle \psi |_\ell c_n^\dagger(t) c_n(t) | \psi \rangle_\ell - \frac{1}{2}. \quad (\text{B.14})$$

can be calculated analytically.

Solving the Heisenberg equation of motion for $\eta_k(t)$ yields $\eta_k(t) = e^{-i\varepsilon_k t} \eta_k$. Using (B.4) then allows to write

$$c_n(t) = \frac{1}{\sqrt{2\pi}} \int_{-\pi}^{\pi} dk e^{ikn} (\alpha_k(t) \eta_k + \beta_k(t) \eta_{-k}^\dagger) \quad (\text{B.15})$$

with $\alpha_k(t) = a_k e^{-i\varepsilon_k t}$ and $\beta_k(t) = -ib_k e^{i\varepsilon_k t}$. Plugging (B.15) and (B.13) into (B.14) yields after some calculation

$$\boxed{\langle \hat{S}^z(n, t) \rangle_\ell = S_{\text{GS}}^z + \frac{I_\ell^A(n, t) - I_\ell^B(n, t)}{(2\pi)^2}}, \quad (\text{B.16})$$

where

$$S_{\text{GS}}^z = \langle 0 | \hat{S}_j^z | 0 \rangle = \frac{1}{2\pi} \int_{-\pi}^{\pi} dk |b_k|^2 - \frac{1}{2} \quad (\text{B.17})$$

is the ground state magnetization and

$$I_\ell^A(n, t) = \left| \int_{-\pi}^{\pi} dk e^{-i[k(\ell-n)+\varepsilon_k t]} (a_k + ib_k) a_k \right|^2 \quad (\text{B.18})$$

$$I_\ell^B(n, t) = \left| \int_{-\pi}^{\pi} dk e^{-i[k(\ell-n)-\varepsilon_k t]} (a_k + ib_k) b_k \right|^2. \quad (\text{B.19})$$

In Appendix D we use (B.16) to compare with results obtained from a CMW simulation.

Appendix C. Analytic Results for the XXZ Model

We derive an exact expression for the group velocities in the XXZ model and calculate the signal velocity v_{\max} .

Appendix C.1. Bethe Ansatz Solution for the ground state

The XXZ model defined by the Hamiltonian

$$H_{\text{XXZ}} = - \sum_j \hat{S}_j^x \hat{S}_{j+1}^x + \hat{S}_j^y \hat{S}_{j+1}^y + \Delta \hat{S}_j^z \hat{S}_{j+1}^z \quad (\text{C.1})$$

can be solved e.g. by means of the coordinate Bethe ansatz [75].

We seek solutions for the ground state and elementary excitations of the XXZ antiferromagnet with $\Delta < -1$ in the thermodynamic limit, which can be found e.g. in [76].

In the thermodynamic limit the roots of the Bethe equations become dense and their distribution for the ground state is characterized by a density function $g_0(x)$, which for $\Delta < -1$ satisfies the following integral equation

$$g_0(x) + \frac{\sinh(2\Phi)}{2\pi} \int_{-\pi}^{\pi} \frac{g_0(x') dx'}{\cosh(2\Phi) - \cos(x-x')} \quad (\text{C.2})$$

$$= \frac{2 \sinh(\Phi)}{\cosh(\Phi) - \cos(x)}, \quad (\text{C.3})$$

where $\cosh(\Phi) = -\Delta$.

The solution to this integral equation is given by

$$g_0(x) = \frac{2K(m_0)}{\pi} \text{dn} \left(\frac{K(m_0)}{\pi} x, m_0 \right), \quad -\pi < x < \pi. \quad (\text{C.4})$$

Here $\text{dn}(x, m)$ is a Jacobian Elliptic Function [77], $K(m)$ the Complete Elliptic Integral of the first kind

$$K(m) = \int_0^{\frac{\pi}{2}} \frac{dx}{\sqrt{1 - m \sin^2 x}} \quad (\text{C.5})$$

and the parameter m_0 the solution of the equation

$$\frac{K(m_0)}{K(1-m_0)} = \frac{\pi}{\Phi}. \quad (\text{C.6})$$

Δ	v_{\max}	Δ	v_{\max}
-1.5	1.78173404	-3.5	1.95920177
-2.0	1.87559502	-4.0	1.96875800
-2.5	1.92014492	-4.5	1.97531255
-3.0	1.94449113	-5	1.98000206

Table C1. Values for the maximum signal velocity v_{\max} in the XXZ model for various values of the interaction strength $\Delta < -1$. These values are obtained from numerically finding the maximum of (C.13) with a numerical precision of 10^{-8} .

The root density $g_0(x)$ can then be used to calculate various quantities such as the ground state energy and elementary excitations.

Appendix C.2. Signal Velocity in the XXZ model

To calculate the maximum signal velocity v_{\max} as a function of Δ we first determine the dispersion relation ε_k for the elementary excitations. As for the TFI model in Appendix B.2 we then obtain v_{\max} as the maximum of the group velocity $v_k = \frac{d\varepsilon_k}{dk}$.

The dispersion of the elementary excitations is given by [76]

$$\varepsilon_k = \frac{1}{2} \sinh(\Phi) [g_0(x_0(k)) - g_0(\pi)] + G(\Delta), \quad (\text{C.7})$$

where $G(\Delta)$ is the finite energy gap present in this phase and $x_0(k)$ has to be determined by inverting

$$k(x_0) = \frac{1}{2} \left(\pi - \int_0^{x_0} g_0(x) dx \right), \quad -\pi \leq x_0 \leq \pi \quad (\text{C.8})$$

for a given momentum k .

From this we can calculate the group velocity

$$v_k = \frac{d\varepsilon_k}{dk} = \frac{d\varepsilon_k}{dx_0} \left(\frac{dk}{dx_0} \right)^{-1} \quad (\text{C.9})$$

where we need

$$\frac{d\varepsilon_k}{dx_0} = \frac{1}{2} \sinh(\Phi) \frac{dg_0}{dx_0}, \quad \frac{dk}{dx_0} = -\frac{g_0(x_0)}{2}. \quad (\text{C.10})$$

Using some properties of Jacobian Elliptic Functions [77] and defining $K_0 = K(m_0)$ we get

$$\frac{dg_0}{dx_0} = -2 m_0 \left(\frac{K_0}{\pi} \right)^2 \operatorname{sn} \left(\frac{K_0 x_0}{\pi}, m_0 \right) \operatorname{cn} \left(\frac{K_0 x_0}{\pi}, m_0 \right) \quad (\text{C.11})$$

where $\operatorname{sn}(x, m)$ and $\operatorname{cn}(x, m)$ are also Jacobian Elliptic functions. Defining

$$S(x_0, K_0, m_0) := \operatorname{sn} \left(\frac{K_0 x_0}{\pi}, m_0 \right) \operatorname{cn} \left(\frac{K_0 x_0}{\pi}, m_0 \right) \quad (\text{C.12})$$

we can then write

$$v_k = \frac{2 m_0 \sinh(\Phi)}{g_0(x_0)} \left(\frac{K_0}{\pi} \right)^2 S(x_0, K_0, m_0). \quad (\text{C.13})$$

We determine the maximum of this function numerically to get v_{\max} as a function of Δ . The values of v_{\max} for various interaction strengths $\Delta < -1$ are listed in table C1 and are obtained with a numerical precision of 10^{-8} .

Appendix D. Test of precision of results

To assess the accuracy of the CMW approach, we compare it with a reference system on a very large lattice and with exact results obtained in Appendix B.3. We investigate simulations of a JW excitation on top of the infinite system ground state in the TFI model at $h = 0.45$ for windows of different sizes, different boundary update methods and different margins between signal and right boundary for triggering the window shift. Note that the correlation length of this system is $\xi \approx 4.36$ sites. It can be obtained from the second largest eigenvalue in magnitude λ_2 of the MPS transfer matrix $T = \sum_s \bar{A}^s \otimes A^s$ as $\xi^{-1} = -\log(|\lambda_2|)$ [4, 78]. For all simulations we use second order Suzuki-Trotter decomposition with time step $\tau = 0.002$ and maximum bond dimension $m_{\max} = 120$. These are the same simulation parameters as used for the investigation of a JW excitation in the TFI model in the main text.

The reference simulation is also performed using the CMW algorithm, but starting with the translation invariant initial state inside a non-moving window of very large size of $N = 1000$ sites. This means that the window is never shifted. Boundary effects are removed by using Method I for *both* boundaries. For the reference simulation we perform time evolution up to $t = 800$, such that the signal induced in the centre of the system at $t = 0$ does not reach the boundaries. For a plot of the reference simulation see figure D1. There we show the transverse magnetization $S^z(n, t)$ and the bipartite entanglement entropy $S_{\text{ent}}(n, t)$. It can be seen that boundary effects are indeed removed for the non-moving window with method I (otherwise disturbances would constantly radiate from the boundaries) and that the signal is still about ≈ 150 sites away from the boundaries at $t = 800$.

We compare results from setups with different CMW sizes N and different numbers of margin sites between signal and right boundary (in sites, see Appendix A.6), as well as different setups for using Method I and II for the updates at the left boundary (LB) and right boundary (RB). We find that the accuracy of the simulation strongly depends on the boundary update method used at the right boundary and the margin between signal and right boundary, whereas the window size N has virtually no impact on the accuracy. For a selection of compared setups see table D1.

For comparison we will consider the transverse magnetization, since only this quantity is available analytically. We display the absolute value of the difference in transverse magnetization,

$$\Delta M(n, t) := |S^z(n, t)_{\text{anal./ref.}} - S^z(n, t)_{[j]}| \quad (\text{D.1})$$

between the reference simulation (ref.) or the analytic result (anal.) (B.16), respectively, and the individual setups $[j]$. We plot this quantity vs. absolute position n at various times $380 \leq t \leq 800$ in figure D2.

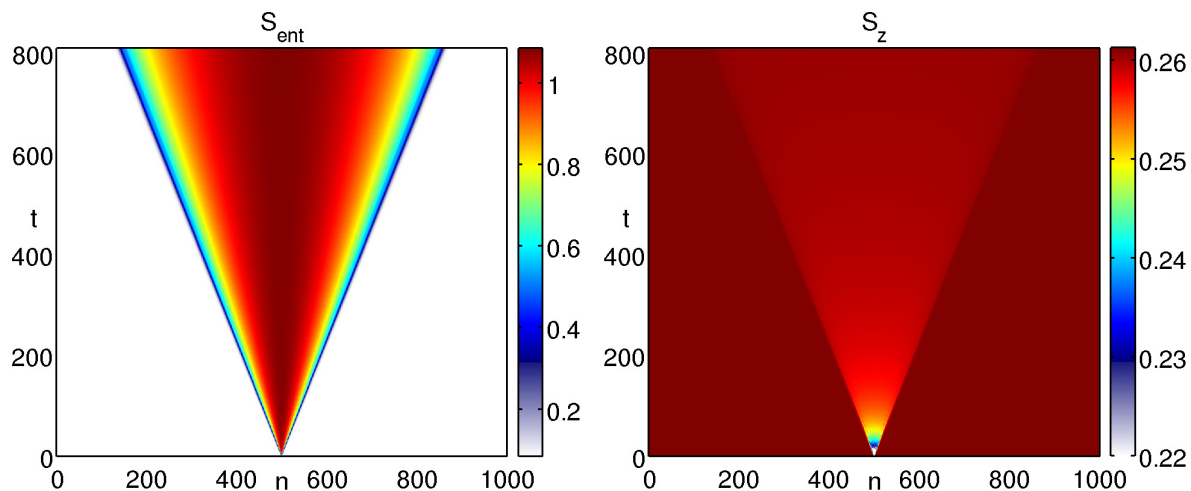


Figure D1. Plot of the reference simulation used for comparison to CMW simulations with different setups described in table D1. The bipartite entanglement entropy $S_{\text{ent}}(n, t)$ and the transverse magnetization $S^z(n, t)$ of a JW excitation in the TFI model at $h = 0.45$ are shown. We use a non-moving window (boundary effects are completely removed by using Method I at both boundaries) with $N = 1000$ sites and perform time evolution using second order Suzuki-Trotter decomposition with time step $\tau = 0.002$ and maximum bond dimension $m_{\text{max}} = 120$ up to $t = 800$.

For other observables, analytic results are not available, but we can compare to the reference simulation. We find that comparison of the magnetization in x direction $S^x(n, t)$ and of the bipartite entanglement entropy $S_{\text{ent}}(n, t)$ to the reference simulation yield results that look very similar to figure D2 and the obtained absolute differences are also of the same orders of magnitude. We note in addition that comparison between left and right column in figure D2 confirms the absence of boundary effects in the reference simulation to high precision.

In the following we discuss the comparisons of the 3 cases listed in table D1.

Case (1) corresponds to the same CMW setup as used for data analysis in the main text. Comparison to the reference simulation yields differences of at most $O(10^{-9})$, whereas a comparison to analytic results yields differences of at most $O(10^{-8})$ everywhere inside the CMW. Around the left boundary differences are of $O(10^{-5})$ for both cases due to perturbations arising from the impinging left going part of the signal. These perturbations however remain confined around the left boundary at all times.

In case (2), where Method II is used at the *right* boundary, differences inside the CMW rise up to $O(10^{-5})$ for both comparisons, i.e. they are considerably higher by about 3-4 orders of magnitude in comparison to case (1), where Method I is used. This can be explained by the fact that Method II breaks the structure of the Suzuki-Trotter decomposition at the boundary, which introduces additional perturbations. These perturbations can in principle be reduced by using higher order Suzuki-Trotter decompositions and smaller time steps and thus increasing computational effort, but they are always present. Method I however is completely devoid of this kind of

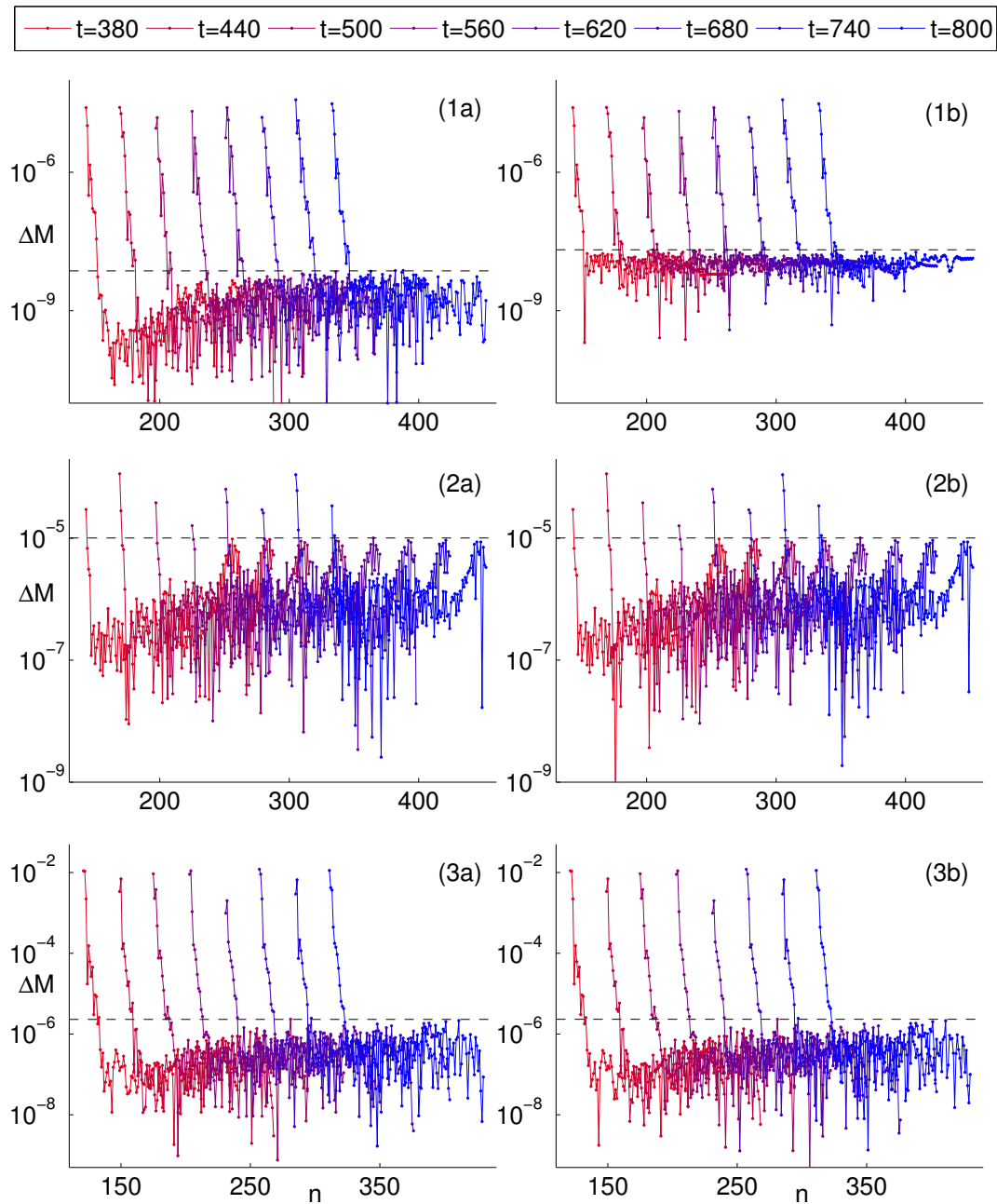


Figure D2. Comparison of results from different selected setups described in table D1 to (a) results from a *reference simulation* (left column) and (b) *analytic results* (B.16) (right column). We plot the absolute differences in measured transverse magnetization $\Delta M(n, t)$ (D.1) vs. absolute position n for various times $380 \leq t \leq 800$. The black dashed lines mark the values of the largest absolute differences inside the CMW away from the left boundary. We note that comparisons of the *longitudinal* magnetization and the entanglement entropy to the reference simulation yield very similar results (not shown).

	N	margin	LB	RB	$P_{\text{ref.}}$	$P_{\text{anal.}}$
(1)	120	24	II	I	7.3×10^{-9}	2.1×10^{-8}
(2)	120	24	II	II	1.0×10^{-5}	1.0×10^{-5}
(3)	120	3	cut	I	2.3×10^{-6}	2.3×10^{-6}
ref.	1000	-	I	I	-	2.0×10^{-8}

Table D1. Precision of different CMW simulation setups, for the case of a JW excitation on top of the infinite system ground state in the TFI model at $h = 0.45$. We compare CMW results on $N = 120$ sites with analytic results (anal.) and with results from a reference simulation on $N = 1000$ sites (ref.). "Margin" specifies the number of sites kept between the signal and the right boundary of the CMW as explained in Appendix A.6. The precision $P_{\text{ref./anal.}}$ is the resulting maximum absolute difference in transverse magnetizations (D.1) inside the CMW away from the left boundary, between the CMW simulation and the reference simulation or analytic result (black dashed lines in figure D2). All simulations were performed using $m_{\text{max}} = 120$ and second order Suzuki-Trotter decomposition with time step $\tau = 0.002$ up to $t = 800$. Case (1) corresponds to the setup used for data analysis in the main text. For (3), "cut" means that the CMW is disconnected from the left part by setting $\hat{h}_{\ell, \ell+1} = 0$, corresponding to the simplest to implement setup, as described in the main text. A comparison between cases (1) and (2) shows that Method I yields very precise results, better by several orders of magnitude than Method II.

perturbations. Also, the renormalized Hamiltonian $H_{r\triangleright}^{\text{eff}}$ necessary for Method II is only calculated up to a finite precision. We however find the perturbations to be largely independent of the precision used to calculate $H_{r\triangleright}^{\text{eff}}$ as described in Appendix A.5. We conclude that using Method I at the right boundary yields results which are better by about 3-4 orders of magnitude in precision than using Method II when employing second order Suzuki-Trotter decomposition with a time step of $\tau = 0.002$.

In case (3) the left part has been disconnected from the CMW altogether by setting $\hat{h}_{\ell, \ell+1} = 0$ ("cut") as described in the main text. Also the margin between signal and right boundary is reduced to 3 sites. Due to the cut, perturbations around the left boundary are now considerably higher and go up to $O(10^{-2})$ both for the comparison to analytic results and the reference simulation. These perturbations however again remain confined around the left boundary at all times. Differences inside the CMW are now $O(10^{-6})$ for both comparisons. This can be explained by the fact that the margin of 3 sites is now smaller than the correlation length $\xi \approx 4.36$ and the exponentially suppressed correlations reaching beyond the Lieb-Robinson light cone [54] induce perturbations at the right boundary.

In conclusion, both Method I (Uniform Update) and Method II (Renormalized Update) work quite well. Furthermore, the easy to implement Method I yields results with a precision of about 10^{-8} , still better by several orders of magnitude than Method II when used at the right boundary. For the methods to work, the margin between signal and right boundary needs to be considerably larger than the correlation length. At the left boundary the easiest approach, a simple cut, already works well when the very rear of the CMW is not of interest.

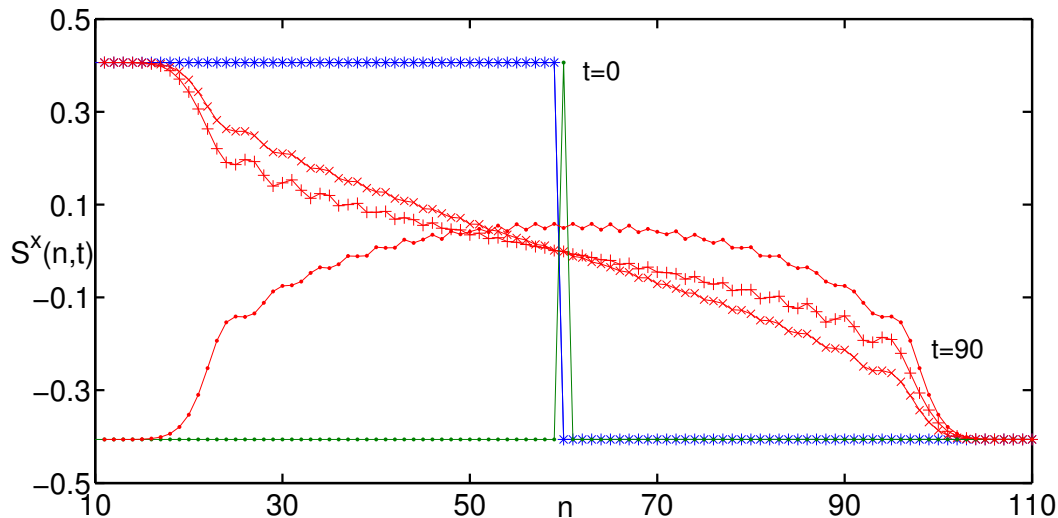


Figure E1. Unscaled magnetization $S^x(n, t)$ of the TFI model at $h = 0.45$ vs. absolute position n . At $t = 90$ (red) from top to bottom on the right side: single spin flip in x -direction (dot symbols), a domain wall excitation (+ symbols), and a JW excitation (x symbols). The initial state at $t = 0$ was a delta spike (green) for the single spin flip and a step function (blue) for the two other excitations.

Overall we have shown that the error produced by the CMW approach, especially with Method I, is very small and remains virtually constant for large times during the simulation when the margin between signal and right boundary is kept sufficiently larger than the correlation length in the initial state.

Appendix E. Unscaled Time Evolution Results

In this Section we show time evolution results before scaling for the TFI model and the XXZ model, for the signals investigated in the main text.

Appendix E.1. TFI model

In our simulations we use a Trotter step size of $\tau = 0.002$ and a maximum matrix dimension $m_{\max} = 120$. The unscaled magnetization $S^x(n, t)$ in the TFI model for the three different quenches employed is shown in figure E1 for times $t = 0$ and $t = 90$. The global shapes are quite different, while developing plateaus are visible for all three quench types at $t = 90$. It can also be seen that around the signal front, the magnetization of a single spin flip is always larger than of a domain wall, which in turn is always greater than the magnetization of a JW excitation. This fact is reflected in the different values for the constant C in figure 3 of the main text.

The unscaled $S^x(n, t)$ at $h = 0.45$ after a JW excitation in the infinite system ground state vs. absolute position n at large times $500 < t < 1000$ is shown in figure E2. The ballistic propagation of the signal front as well as magnetization steps near the front are clearly visible. No such steps appear in the transverse magnetization. A

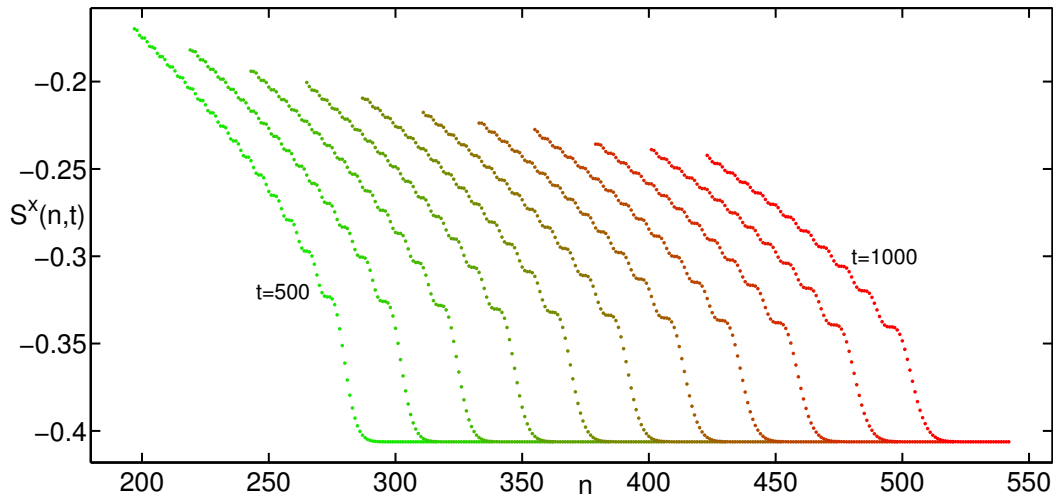


Figure E2. Unscaled magnetization $S^x(n, t)$ of the TFI model at $h = 0.45$ vs. absolute position n after a JW excitation for times $500 < t < 1000$ in time steps of 50.

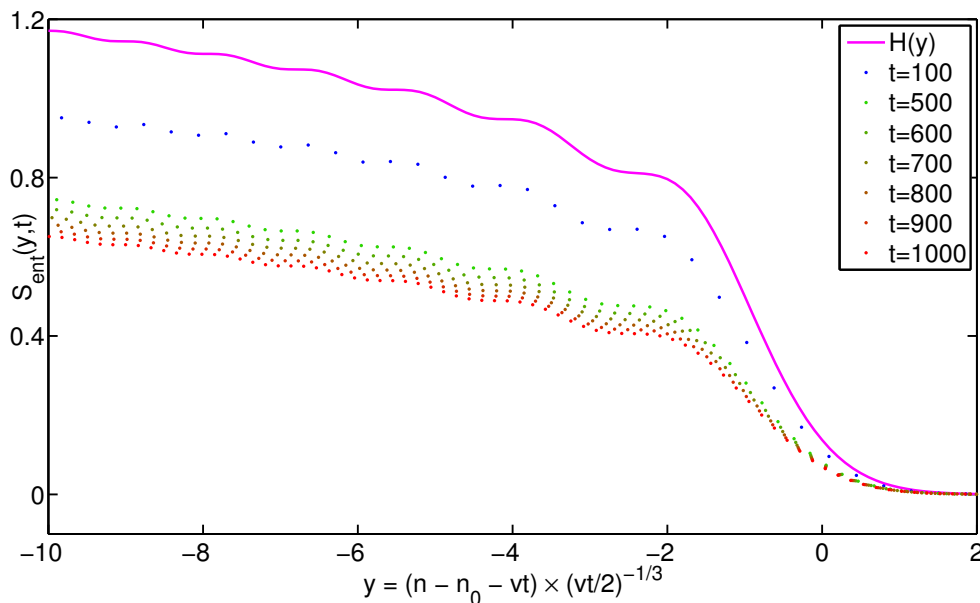


Figure E3. Unscaled bipartite entanglement entropy $S_{\text{ent}}^{\text{TFI}}(y, t)$ of the TFI model $h = 0.45$ after a JW excitation vs. scaled position y , which is at all times smaller than the entanglement entropy $S_{\text{ent}}^{\text{TB}}(y, t)$ for tight binding fermions, which approaches the scaling function $H(y)$ without any scaling (c.f. figure 3 in [44])

scaling behaviour of the magnitude and distance to the signal front of the steps can be conjectured. This scaling behaviour is discussed in detail in the main text.

Other observables and signals, such as single spin flip and domain wall excitations qualitatively show the same propagation, shape and step structure. Their scaling behaviour however varies in scaling exponents and quality with varying field strength h .

We also show the bipartite entanglement entropy $S_{\text{ent}}^{\text{TFI}}(n, t)$ after a JW excitation

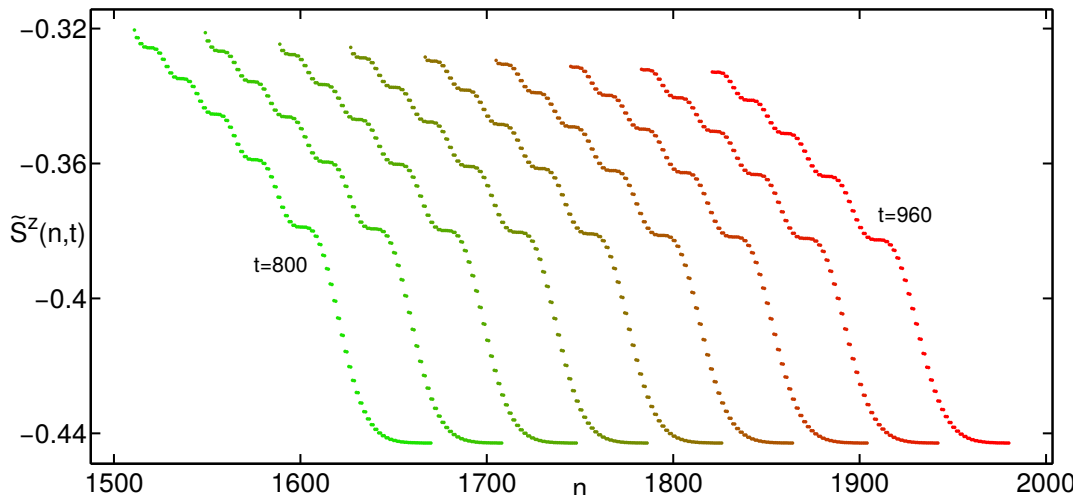


Figure E4. Unscaled staggered magnetization $\tilde{S}^z(n, t)$ of the XXZ model at $\Delta = -3$ after a JW excitation vs. absolute position n at times $800 < t < 960$ in time steps of 20.

at $h = 0.45$ in figure E3. It is smaller than the entanglement entropy for tight binding fermions after a domain wall excitation at all times. In the latter case, $S_{\text{ent}}^{\text{TB}}(n, t)$ approaches the asymptotic scaling function $H(y)$ *without* any scaling in time. In fact, $S_{\text{ent}}^{\text{TFI}}(n, t)$ decreases in time, whereas $S_{\text{ent}}^{\text{TB}}(n, t)$ approaches $H(y)$ from below. The exact relation between the scaled excess longitudinal magnetization $M(n, t) = (S^x(n, t) - S_{\text{GS}}^x)/|2S_{\text{GS}}^x|$ and the fermion density $N_{\text{TB}}(n, t)$ described in the main text therefore does not carry over to the entanglement entropy.

Appendix E.2. XXZ model

For the XXZ simulations we use a Trotter step size of $\tau = 0.01$ and maximum matrix dimensions of $m_{\text{max}} = 150$ for $\Delta = -4$, $m_{\text{max}} = 160$ for $\Delta = -3$ and $m_{\text{max}} = 180$ for $\Delta = -2$. We show a representative plot of the unscaled staggered magnetization $\tilde{S}^z(n, t) = (-1)^n S^z(n, t)$ at $\Delta = -3$ after a JW excitation on top of the infinite system ground state vs. absolute position n at various times $800 < t < 960$ in figure E4. Again we observe a ballistic propagation of the signal front as well as magnetization steps near the front as in the TFI model case. For the XXZ model an additional micro step structure appears due to “pairing” of neighbouring sites, which is due to the spinon nature of the elementary excitations created by the signal (see section 3.2).

The scaling behaviour of the larger step structure is investigated in detail in the main text. The overall shape of the unscaled staggered magnetization $\tilde{S}^z(n, t)$ looks similar to the shape of the longitudinal magnetization $S^x(n, t)$ of the TFI model with a JW excitation as shown in figure E1. Different signals such as single spin flips yield similar results.

Appendix F. Boundary Reflections

In this appendix we consider the case of signals impacting the boundaries of a non-moving window for several different models. We study the time evolution beyond the time where a signal reaches the boundaries, both with Method I and Method II. In *all* cases we observe reflections from the boundary after some time. The nature of these reflections generally depends on the boundary update method as well as the initial uniform state and the type of the signal.

The models and signals that have been studied in particular are the TFI model with a JW excitation and a single spin flip in x -direction, the XXZ model with a JW excitation and a single spin flip in z -direction, the $S = 1$ Heisenberg model with a spin up excitation (this particular case is also studied in [50] with a method similar to Method II, but only for shorter times), and the $S = 1$ AKLT model [64] with a spin up excitation. We observe reflections from the boundary after some time in *all* cases.

In the following we show results for the two cases of the TFI model with a JW excitation and the $S = 1$ AKLT model with a spin up excitation, where we have used Method II for the left boundary and Method I for the right boundary to see their respective behaviour.

Appendix F.1. TFI model with JW excitation

We again consider the TFI model at $h = 0.45$ after a JW excitation in the infinite system ground state. We use a non-moving window with $N = 50$ and maximum bond dimension $m_{\max} = 120$, where the ground state MPS representation has bond dimension $m_0 = 30$. The time evolution of the bipartite entanglement entropy $S_{\text{ent}}(n, t)$ and the magnetization $S^x(n, t)$ can be seen in figure F1. The signal reaches the boundaries at $t \approx 40$ and reflections start to emerge at $t \approx 90$.

We compare the magnetization $S^x(n, t)$ of this simulation with the magnetization $S_{\text{ref}}^x(n, t)$ of the reference simulation of Appendix D and show their absolute difference $\Delta M(n, t) = |S^x(n, t) - S_{\text{ref}}^x(n, t)|$ in figure F2, where subplot (a) shows $\Delta M(n, t)$ at the left and right boundaries of the $N = 50$ non-moving window ($n = 1$ and $n = 50$ respectively) vs. time t and subplot (b) shows $\Delta M(n, t)$ vs. position n inside the non-moving window at various times t .

In figure F2(a) it can be seen that initially the deviations at the right side (Method I) are much lower than at the left side (Method II) until $t \approx 50$. The deviation at both boundaries then increases exponentially further until $t \approx 100$, where it becomes of the order $O(1)$. We notice that the deviations for the right boundary are always a bit lower than for the left boundary. We conclude that for the investigated case Method I performs slightly better than Method II in absorbing a signal for a limited time.

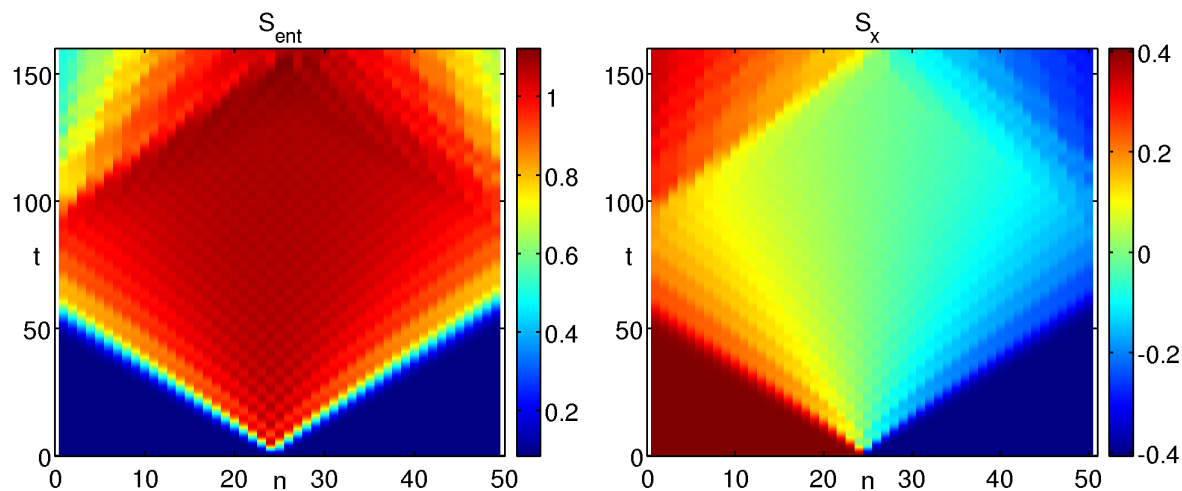


Figure F1. Time evolution of the bipartite entanglement entropy $S_{\text{ent}}(n, t)$ (left) and the magnetization $S^x(n, t)$ (right) in the TFI model at $h = 0.45$ after a JW excitation within a non-moving CMW of size $N = 50$. Time evolution is continued after the signal has impacted the boundaries at $t \approx 40$. Reflections emerge at $t \approx 90$ at both boundaries, where we use Method I at the right and Method II at the left boundary.

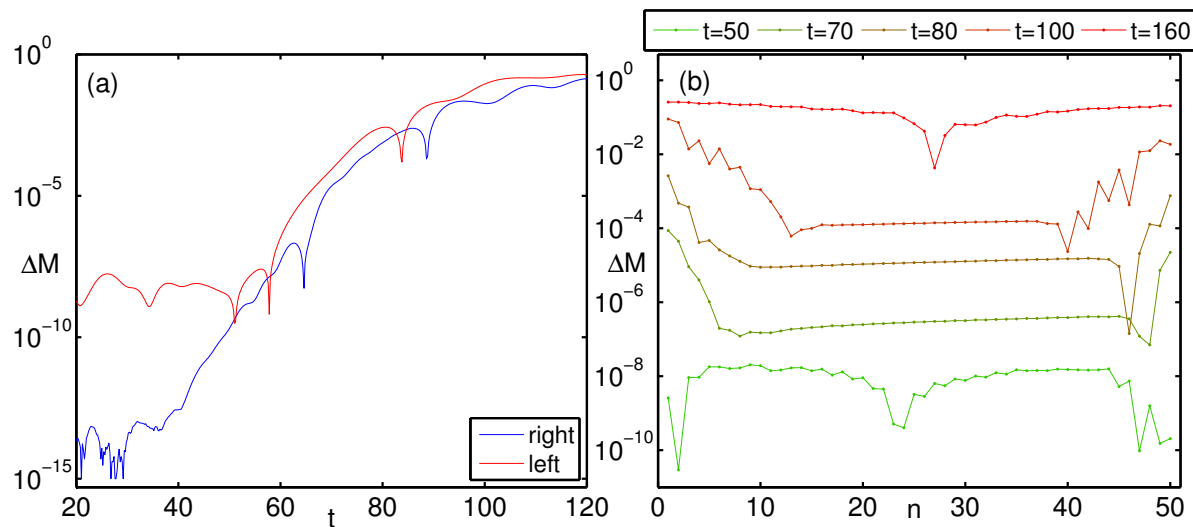


Figure F2. Difference $\Delta M(n, t) = |S^x(n, t) - S_{\text{ref}}^x(n, t)|$ between magnetization $S^x(n, t)$ of figure F1 and magnetization $S_{\text{ref}}^x(n, t)$ of the reference simulation of Appendix D. (a) Difference at the immediate left and right boundaries of the $N = 50$ non-moving window ($n = 1$ and $n = 50$ respectively) vs. time t . (b) Difference $\Delta M(n, t)$ vs. position n inside the non-moving window for various times t .

Appendix F.2. AKLT model with spin up excitation

We also consider the $S = 1$ bilinear, biquadratic chain at the *AKLT* point [64] defined by the Hamiltonian

$$\hat{H} = \sum_j \hat{\mathbf{S}}_j \cdot \hat{\mathbf{S}}_{j+1} + \frac{1}{3} (\hat{\mathbf{S}}_j \cdot \hat{\mathbf{S}}_{j+1})^2. \quad (\text{F.1})$$

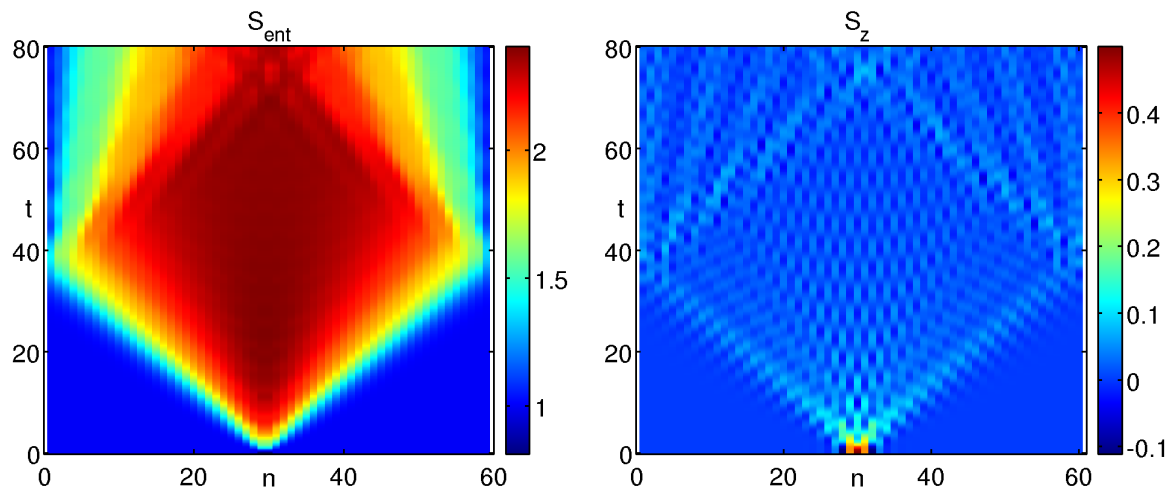


Figure F3. Time evolution of the bipartite entanglement entropy $S_{\text{ent}}(n, t)$ (left) and the magnetization $S^z(n, t)$ (right) in the AKLT model after an excitation induced by $\hat{S}_{n_0}^+$ on top of the infinite system ground state within a non-moving CMW of size $N = 60$. Time evolution is continued after the signal has impacted the boundaries at $t \approx 35$ to follow reflections which emerge almost immediately.

The ground state is a valence bond state and has an exact MPS representation with bond dimension $m_0 = 2$ (see e.g. [5]). We induce a signal on top of the infinite system ground state by applying the spin ladder operator $S_{n_0}^+$. We use a non-moving window with $N = 60$ sites and maximum bond dimension $m_{\text{max}} = 200$. The time evolution of the bipartite entanglement entropy $S_{\text{ent}}(n, t)$ and the magnetization $S^z(n, t)$ can be seen in figure F3.

Here the signal impacting at $t \approx 35$ is reflected almost immediately. This stems from the fact that the MPS matrices at the boundary sites have to absorb all the information about excited states contained within the propagating signal. Here these matrices however have bond dimension $m_0 = 2$ which is much too small for the matrices to absorb this information for a long time span.

References

- [1] M. Cheneau, P. Barmettler, D. Poletti, M. Endres, P. Schauß, T. Fukuhara, Ch. Gross, I. Bloch, C. Kollath, S. Kuhr, *Nature* **481**, 484 (2012).
- [2] R. Varga, K. L. Garcia, M. Vázquez, P. Vojtanik, *Phys. Rev. Lett.* **94**, 017201 (2005).
- [3] M. Fannes, B. Nachtergaele, R. Werner, *Comm. Math. Phys.* **144**, 443 (1992)
- [4] F. Verstraete, V. Murg, J.I. Cirac, *Adv. Phys.* **57**, 143 (2008);
- [5] U. Schollwöck, *Annals of Physics* **326**, 96 (2011).
- [6] S.R. White, *Phys. Rev. Lett.* **69**, 2863 (1992); *Phys. Rev. B* **48**, 10345 (1993).
- [7] G. Vidal, *Phys. Rev. Lett.* **91**, 147902 (2003); *ibid* **93**, 040502 (2004).
- [8] S.R. White, A.E. Feiguin, *Phys. Rev. Lett.* **93**, 076401 (2004); A.E. Feiguin, S.R. White, *Phys. Rev. B* **72**, 020404 (2005); A.J. Daley, C. Kollath, U. Schollwöck, G. Vidal, *J. Stat. Mech.: Theor. Exp.*, P04005 (2004).
- [9] P. Calabrese, J. Cardy, *J. Stat. Mech.* **06**, P06008 (2007).
- [10] P. Calabrese, F.H.L. Essler, M. Fagotti, *Phys. Rev. Lett.* **106**, 227203 (2011); *J. Stat. Mech.* (2012) P07016
- [11] F. Iglói, H. Rieger, *Phys. Rev. Lett.* **85**, 3233 (2000).
- [12] F. Iglói, H. Rieger, *Phys. Rev. Lett.* **106**, 035701 (2011).
- [13] H. Rieger, F. Iglói, *Phys. Rev. B* **84**, 165117 (2011).
- [14] V. Eisler, F. Iglói, I. Peschel, *J. Stat. Mech.* (2009) P02011 .
- [15] D. Rossini, A. Silva, G. Mussardo, G. E. Santoro, *Phys. Rev. Lett.* **102**, 127204 (2009).
- [16] D. Rossini, S. Suzuki, G. Mussardo, G. E. Santoro, A. Silva, *Phys. Rev. B* **82**, 144302 (2010).
- [17] L. Foini, L.F. Cugliandolo, A. Gambassi, *Phys. Rev. B* **84**, 212404 (2011).
- [18] D. Schuricht, F.H.L. Essler, *J. Stat. Mech.* (2012) P04017.
- [19] P. Barmettler, M. Punk, V. Gritsev, E. Demler, E. Altman, *Phys. Rev. Lett.* **102**, 130603 (2009); *N. J. Phys.* **12**, 055017 (2010).
- [20] M. Fagotti, F.H.L. Essler, *J. Stat. Mech.* **07**, P07012 (2013).
- [21] M. Fagotti, M. Collura, F.H.L. Essler, P. Calabrese, *Phys. Rev. B* **89**, 125101 (2014)
- [22] F. Pollmann, M. Haque, B. Dóra, *Phys. Rev. B* **87**, 041109(R) (2013)
- [23] M. Brockmann et al., *J. Stat. Mech.* (2014) P12009
- [24] D. Karevski, *Eur. Phys. J. B* **27**, 147 (2002).
- [25] T. Platini, D. Karevski, *Eur. Phys. J.* **B48**, 225 (2005); *J. Phys. A: Math. Theor.* **40**, 1711 (2007).
- [26] V. Eisler, D. Karevski, T. Platini, I. Peschel, *J. Stat. Mech.* **01**, P01023 (2008).
- [27] U. Divakaran, F. Iglói, H. Rieger, *J. Stat. Mech.* **10**, P10027 (2011).
- [28] D. Gobert , C. Kollath, U. Schollwöck, G. Schütz, *Phys. Rev. E* **71**, 036102 (2005).
- [29] R.G. Pereira, S.R. White, I. Affleck, *Phys. Rev. Lett* **100**, 027206 (2008).
- [30] S. Langer, F. Heidrich-Meisner, J. Gemmer, I.P. McCulloch, U. Schollwöck, *Phys. Rev. B* **79**, 214409 (2009); S. Langer, M. Heyl, I.P. McCulloch, F. Heidrich-Meisner, *Phys. Rev. B* **84**, 205115 (2011).
- [31] J. Lancaster, A. Mitra, *Phys. Rev. E* **81**, 061134 (2010).
- [32] J. Mossel, J.-S. Caux, *N. J. Phys.* **12**, 055028 (2010).
- [33] M. S. Foster, T. C. Berkelbach, D. R. Reichman, E. A. Yuzbashyan, *Phys. Rev. B* **84**, 085146 (2011).
- [34] S. Jesenko, M. Znidaric, *Phys. Rev. B* **84**, 174438 (2011).
- [35] M. Ganahl, E. Rabel, F.H.L. Essler, H.G. Evertz, *Phys. Rev. Lett.* **108**, 077206 (2012).
- [36] V. Alba, F. Heidrich-Meisner, *Phys. Rev. B* **90**, 075144 (2014)
- [37] C. Karrasch, J. E. Moore, F. Heidrich-Meisner, *Phys. Rev. B* **89**, 075139 (2014)
- [38] T. Sabetta and G. Misguich, *Phys. Rev. B* **88**, 245114 (2013).
- [39] J. C. Halimeh, A. Wöllert, I. McCulloch, U. Schollwöck, and T. Barthel, *Phys. Rev. A* **89**, 063603 (2014).
- [40] D.B. Abraham, E. Barouch, G. Gallavotti, and A. Martin-Löf, *Phys. Rev. Lett.* **25**, 1449 (1970)

- [41] T. Antal, Z. Rácz, A. Rákos, G.M. Schütz, Phys. Rev. E **59**, 4912 (1999).
- [42] V. Hunyadi, Z. Rácz, L. Sasvári, Phys. Rev. E **69**, 066103 (2004).
- [43] T. Antal, P. L. Krapivsky, A. Rakós, Phys. Rev. E **78**, 061115 (2008).
- [44] V. Eisler, Z. Rácz, Phys. Rev. Lett. **110**, 060602 (2013).
- [45] N. Schuch, M.M. Wolf, K.G.H. Vollbrecht, J.I. Cirac, New J. Phys. **10**, 033032 (2008).
- [46] T. Prosen, M. Znidaric, Phys. Rev. E **75**, 015202 (2007).
- [47] G. Vidal, Phys. Rev. Lett. **98**, 070201 (2007).
- [48] I.P. McCulloch, arXiv:0804.2509 (2008).
- [49] J. Haegeman et al., Phys. Rev. Lett. **107**, 070601 (2011)
- [50] H.N. Phien, G. Vidal, I.P. McCulloch, Phys. Rev. B **86**, 245107 (2012)
- [51] H.N. Phien, G. Vidal, I.P. McCulloch, Phys. Rev. B **88**, 035103 (2013)
- [52] A. Milsted, J. Haegeman, T.J. Osborne, F. Verstraete, Phys. Rev. B **88**, 155116 (2013)
- [53] The original preprints of [50, 51, 52] (arXiv:1207.0652, 1207.0678, 1207.0691) and of the present work (arXiv:1207.0862) appeared at the same time.
- [54] E.H. Lieb, D.W. Robinson, Comm. Math. Phys. **28**, 251 (1972); B. Nachtergaele, R. Sims, Comm. Math. Phys. **265**, 119 (2006)
- [55] T. Barthel, M. Kliesch, Phys. Rev. Lett. **108**, 230504 (2012).
- [56] L. Amico, A. Osterloh, F. Plastina, R. Fazio, G.M. Palma, Phys. Rev. A **69**, 022304 (2004).
- [57] L. Amico, R. Fazio, A. Osterloh, V. Vedral, Rev. Mod. Phys. **80**, 517 (2008).
- [58] H.F. Trotter, Proc. Am. Math. Soc. **10**, 545 (1959). M. Suzuki, Prog. Theor. Phys. **56**, 1454 (1976).
- [59] M.A. Cazalilla, J.B. Marston, Phys. Rev. Lett. **88**, 256403 (2002); *ibid.* **91**, 049702 (2003).
- [60] E.H. Lieb, T. Schultz, D. Mattis, Ann. Phys. **16**, 407 (1961).
- [61] P. Pfeuty, Ann. Phys. **57**, 79 (1970)
- [62] P. Jordan, E. Wigner, Z. Phys. **47**, 631 (1928).
- [63] H. Rieger (private communication)
- [64] I. Affleck, T. Kennedy, E.H. Lieb, H. Tasaki, Phys. Rev. Lett. **59**, 799 (1987).
- [65] K. Okunishi, T. Nishino, Phys. Rev. B **82**, 144409 (2010).
- [66] H. Ueda, T. Nishino, J. Phys. Soc. Jpn. **78**, 014001 (2009).
- [67] M.B. Hastings, J. Math. Phys. **50**, 095207 (2009).
- [68] R. J. Bursill, T. Xiang, G. A. Gehring, J. Phys. Cond. Mat. **8** (1996) L583; X. Wang, T. Xiang, Phys. Rev. B **56**, 5061 (1997); N. Shibata, J. Phys. Soc. Jpn. **66**, 2221 (1997).
- [69] F. Verstraete, J.J. Garcia-Ripoll, J.I. Cirac, Phys. Rev. Lett. **93**, 207204 (2004);
- [70] I.P. McCulloch, J. Stat. Mech.: Theor. Exp. (2007) P10014;
- [71] B. Pirvu, V. Murg, J.I. Cirac, F. Verstraete, New J. Phys. **12**, 025012 (2010)
- [72] G.M. Crosswhite, D. Bacon, Phys. Rev. A **78**, 012356 (2008); G.M. Crosswhite, A.C. Doherty, G. Vidal, Phys. Rev. B **78**, 035116 (2008); F. Fröwis, V. Nebendahl, W. Dür, Phys. Rev. A **81**, 062337 (2010)
- [73] L. Michel, I.P. McCulloch, arXiv:1008.4667 (2010)
- [74] N. Bogoliubov, J. Phys. (USSR) **11**, 23 (1947).
- [75] H. Bethe, Z. Phys. **71**, 205 (1931)
- [76] J. des Cloizeaux, M. Gaudin, J. Math. Phys. **7**, 1384 (1966)
- [77] M. Abramowitz, I. Stegun, *Handbook of Mathematical Functions*, Dover Publications, 1965
- [78] S. Östlund, S. Rommer, Phys. Rev. Lett. **75**, 3537 (1995)